coatings

*Article*

# Simulations of Effects of Geometric and Material Parameters on the Interfacial Stress of the Thermal Barrier Coatings with Free Edges

**Qiannan Tao [1], Yanrong Wang [1,2], Shun Yang [1] and Yihui Liu [1,*]**

[1] School of Energy and Power Engineering, Beihang University, Beijing 100191, China; lea_qiannan@buaa.edu.cn (Q.T.); yrwang@buaa.edu.cn (Y.W.); yangshun_academic@outlook.com (S.Y.)
[2] Jiangxi Research Institute, Beihang University, Nanchang 330096, China
* Correspondence: yihui_liu@buaa.edu.cn

**Abstract:** Interfacial stress between layers of thermal barrier coatings near free edges is a critical factor that may cause turbine blades to fail. This paper uses simulation methods to reveal the effects of variations in geometric and material parameters on the stress of thermal barrier coatings. The stress distributions of a disk-shaped coating–substrate system undergoing thermal mismatch are calculated by an analytical method and the finite element method. The analytical solution reveals that the coefficient of thermal expansion, elasticity modulus, Poisson's ratio, and thickness of each layer affect interfacial stress between coatings and substrate. The simulation results exhibit significant concentrations of the normal and shear stresses, which make the coating system prone to cracking and spalling from the free edge. The parametric analysis highlights that the thermal mismatch strain affects the stress magnitude. The region affected by free edges becomes larger with increasing thickness, elasticity modulus, and Poisson's ratio of the topcoat. Finally, two integral parameters are proposed to represent the stress state near the free edge related to mode I and II fracture, respectively. The parameters, not sensitive to the grid density, are validated by experiments.

**Keywords:** thermal barrier coatings; thermal growth oxidation; interfacial stress; thermal mismatch; free edge effect



**Citation:** Tao, Q.; Wang, Y.; Yang, S.; Liu, Y. Simulations of Effects of Geometric and Material Parameters on the Interfacial Stress of the Thermal Barrier Coatings with Free Edges. *Coatings* **2023**, *13*, 1378. https://doi.org/10.3390/coatings13081378

Academic Editor: Narottam Bansal

Received: 6 July 2023
Revised: 30 July 2023
Accepted: 4 August 2023
Published: 6 August 2023



## 1. Introduction

The improvement in gas turbine efficiency increases the gas temperature and working pressure, which places a large demand on the blade materials. The introduction of thermal barrier coatings (TBCs) is one of the most effective ways to ensure that turbine blades can work reliably and stably under elevated thermal conditions [1–3].

TBCs are sprayed on turbine blades to provide thermal insulation. The exterior surface of the coating directly faces the thermal gas, and it firmly adheres to the substrate [4–6]. The coating has a complex multilayer structure, although it is only a few hundred microns thick [7–9]. Additionally, the film cooling holes, blade tips, and platform of turbine blades destroy the structural continuity of TBCs, thus introducing many free edges, which are considered to be the vulnerable spots where TBCs fail prematurely and undergo complicated failure modes [10,11]. Accordingly, potential locations where spalling may occur in a thermal barrier-coated turbine blade are shown in Figure 1.

As indicated, a TBC is a complex multilayer system that consists of a topcoat (TC), bondcoat (BC), and substrate as well as thermally grown oxidation (TGO) between the BC and TC. The layers have different thermomechanical properties. That is, the significant differences in thermal conductivity and coefficient of thermal expansion (CTE) between the TC (machined from ceramic) and substrate lead to thermal mismatch deformation between layers and introduce severe thermal mismatch stress between layers [12–14]. Therefore, it is of great engineering significance to accurately analyze the stress on the interface of layers near the free edges of TBCs to reasonably evaluate the performance and reliability of TBC systems.

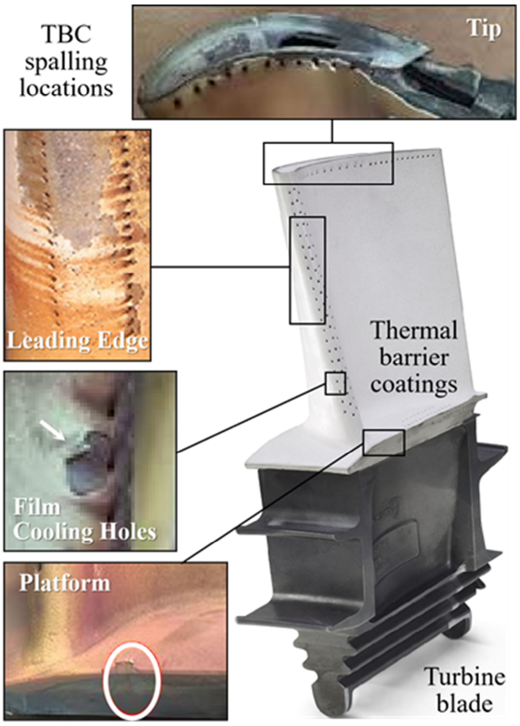


**Figure 1.** Potential spalling locations in a thermal barrier coated turbine blade.

To obtain the stress in multilayer systems, considerable effort has been devoted to constructing analytical solutions. The first documented method for calculating stress inside a film-substrate system was proposed by Stoney [15] as early as the 1900s. In his study, the mismatch stress was suggested to be $\sigma = E_s H_s^2 / \left(6 H_f \rho^2\right)$, where $E_s$, $E_f$, $H_s$, $H_f$, are the elastic modulus and thickness of the substrate and film, respectively. As presented, the stress is supposed to be negatively correlated with the squared radius of curvature $\rho^2$. Stoney's equation was only applicable when the coating thickness was much less than the substrate thickness [16]. Although this empirical expression does not reflect the mechanical mechanism of all multilayer systems, its engineering practicability and applicability are acceptable [17–19]. Afterwards, based on beam theory and the concept of interfacial compliance, Suhir [20,21] developed a novel method that works well for both multilayered heteroepitaxial structures and circular substrate-thin film structures. The method proposed by Suhir based on beam theory is of particular mechanical significance. It is proven to be especially applicable to describe the interfacial stress of film/substrate systems [22,23]. However, Suhir's method fails to accurately describe thick coatings. Teixeira [24] proposed a simple equation similar to Suhir's method to estimate the thermal stress due to the CTE mismatch and temperature difference. Following the algorithm presented in the work of Hu [25], the stress field near the free edge was well expressed by the finite difference method. However, the equations of Teixeira [24] cannot give reasonable solutions for thick coatings. Considering multilayer systems with an uncertain number of layers, Hsueh [26] introduced a practical method. Hsueh divided the strain parallel to the interface into a uniform strain component and a bending strain component and introduced three boundary conditions to obtain a closed-form solution. In this method, the compatibility condition between layers is naturally satisfied. Furthermore, there are only three unknowns and three boundary conditions regardless of the number of layers [27]. Subsequently, Hu and Huang [28,29] further expanded the models to the elastoplastic category. A closed-form solution for analyzing the inner stress in a thin film-substrate system was suggested and proved to be more practical than the elastic solution, although the closed-form model cannot give a free edge solution with reasonable physical significance. Following the study of Hu and Huang, Gao et al. [30] derived a very simplified closed-form solution regarding film stress. Recently, Jiang et al. [10] further developed the method proposed by Hsueh and predicted the residual stress in a TBC-film cooling system. Meng et al. [31] introduced an optimized analytical model considering a nonuniform temperature field that enabled the use of a theoretical model to describe the service reliability of coated turbine blades in engineering practice. Studies by Tsui and Clyne [32–34], Moore [35], Widjaja et al. [36], and Jiang et al. [37], utilized analytical methods to obtain more reasonable and accurate solutions for TBC systems. A summary of previous studies on the mismatch stress is listed in Table 1 and Appendix A.

**Table 1.** Review of the studies on stress due to thermal mismatch.

| Reference | Structure | Method | Acquired Value | | | |
|---|---|---|---|---|---|---|
| | | | Normal Stress Parallel to Interface | Shear Stress | | Interfacial Normal Stress |
| | | | | Yes or No | Whether $\tau_{\mathrm{edge}} = 0$ Is Met | |
| [15] | a thin-film bilayer system | A.S. | yes | no | - | no |
| [20] | a multilayered heteroepitaxial structure | A.S. | yes | yes | no | yes |
| [21] | a circular thin-film substrate structure | A.S. | yes | yes | no | yes |
| [24] | a ceramic-metal bilayer | A.S. | yes | no | - | no |
| [26] | a multilayered elastic strip with a planar geometry | A.S. | yes | no | - | no |
| [28] | a planar geometry | A.S. | yes | no | - | no |
| [27] | a planar geometry | A.S. and FEM | yes | yes | no | no |
| [30] | an elastic multilayer coating system | A.S. | yes | no | - | no |
| [10] | a disk with one hole in the middle | A.S. and FEM | yes | no | - | no |
| [31] | a disk with one hole in the middle | A.S. | yes | yes | no | no |

A.S. is an abbreviation for the analytical solution. FEM is an abbreviation for the finite element method.

Few of the analytical methods for solving the stress of multilayer structures could meet the following boundary conditions: (1) the shear stress equals zero at the free edge, and (2) the maximum shear stress occurs at a point close to the free edge of the coating but not at the edge itself [38]. One analytical model meeting these conditions is based on the sinusoidal form of the shear stress distribution, $\tau = \tau_{\max} \sin(2\pi x/l)$ [39]. However, the sinusoidal distribution is not suitable for TBC systems. Since the analytical method has many limitations and is difficult to apply to complex systems, the finite element method (FEM) is widely used to study the stress state of coating–substrate systems.

Few quantitative analyses have been conducted on the interfacial stress in coating–substrate systems near the free edge. However, spalling of the coating from the edge is mainly due to the interfacial stress near the free edge. This paper aims to analyze the effects of geometric and material variations on the interfacial stress near the free edge of coating–substrate systems and to propose some representative parameters that can describe the interfacial stress distribution in coating–substrate systems. To facilitate force analysis, a thin elastic disk with a TBC is chosen as the simulation object since the disk hoop stress due to thermal mismatch is self-balancing. An analytical solution for normal stress parallel to the interface in a thick coating–substrate system is proposed, and expressions for the relationships of interfacial stress and normal stress are found. Based on the expressions, we determine which material and geometric characteristics affect the interfacial stress between layers and then use the FEM to determine how they affect the stress. We propose a nondimensional parameter to determine the range affected by the free edge and propose two integral parameters to represent the stress state near the free edge. The larger the value of the integral, the more likely the TBC system is to fail. The experimental results are consistent with the predicted trend.

## 2. Theoretical Deduction and Numerical Simulation

The TBC was applied on the disk-shaped superalloy substrate, as shown in Figure 2. The scanning electron microscopy (SEM) images in Figure 2 illustrate that the disk can be modeled as an axisymmetric multilayer system. Figure 3a presents the geometry of the analytical model as well as the coordinate system for analysis. From the SEM images in Figure 2, the interface between each layer in the TBC is curving, but it is difficult to model due to the irregular interface topography. Considering that the curvature of the interface is not an essential factor in the interfacial failure near the edge, the interface is assumed to be straight to simplify the problem.

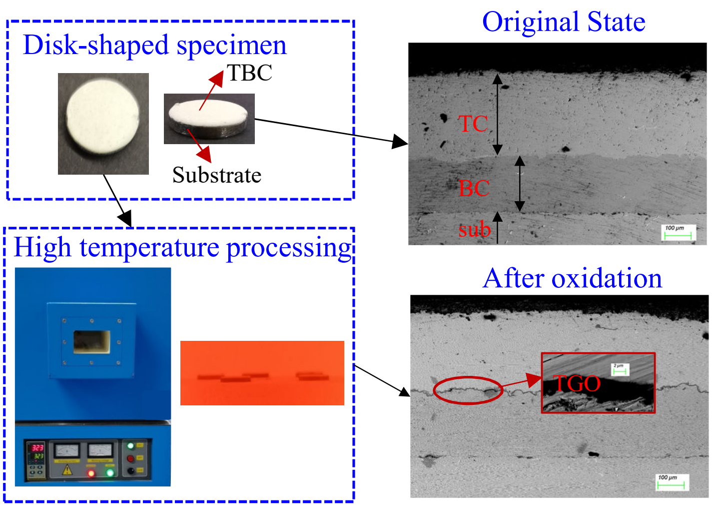


**Figure 2.** The disk-shaped superalloy sample with TBC and the SEM image of the original state and the oxidized state of the TBC.

When the operating temperature $T_{\mathrm{op}}$ deviates from the stress-free temperature $T_{\mathrm{sf}}$, the radial stress $\sigma_x$ and hoop stress $\sigma_z$ are not 0 due to the different thermal strains of the separate materials. The thermal strain can be calculated by $\varepsilon_i^{\mathrm{t}} = \alpha_i \Delta T$, where $\alpha$ is the CTE and $\Delta T = T_{\mathrm{op}} - T_{\mathrm{sf}}$. The hoop stress is self-balancing, and the radial stress can be balanced by interfacial shear stress $\tau$ between two layers. Bending deformation should occur in the disk, and the term $M(\zeta)$ in Figure 3a represents the moment caused by the bending of the layer. To satisfy the equilibrium moment at point $P_1$, there should be interfacial normal stress between the layers, indicated as $\sigma_\mathrm{n}$ in Figure 3a. Taking part of the TC layer near the edge as an analytical object, the equilibrium equations in the radial direction ($x$-direction) and axial direction ($y$-direction) are Equations (1) and (2), respectively. The equilibrium equation of the moment at point $P_1$ is written as Equation (3) and the equilibrium equation of the moment at point $P_2$ is written as Equation (4),

$$\int_0^{H_{\mathrm{TC}}} \sigma_x(\zeta)\zeta \mathrm{d}y + \int_\zeta^R \int_0^{H_{\mathrm{TC}}} \sigma_z(x,y)\mathrm{d}x\mathrm{d}y - \int_\zeta^R \tau(x)x\mathrm{d}x = 0 \tag{1}$$

$$\int_0^R \sigma_\mathrm{n}(x)x\mathrm{d}x = 0 \tag{2}$$

$$-\int_0^{H_{\mathrm{TC}}} \sigma_\zeta(y)\zeta y\, \mathrm{d}y + M(\zeta) + \int_\zeta^R \sigma_\mathrm{n}(x)x(x-\zeta)\mathrm{d}x = 0 \tag{3}$$

$$-\int_0^{H_{\mathrm{TC}}} \sigma_\zeta(y)\zeta y\, \mathrm{d}y + M(\zeta) - \int_\zeta^R \sigma_\mathrm{n}(x)x(R-x)\mathrm{d}x = 0 \tag{4}$$

where $R$ is the radius of the disk, and the cross-section is located at the point $x = \zeta$.

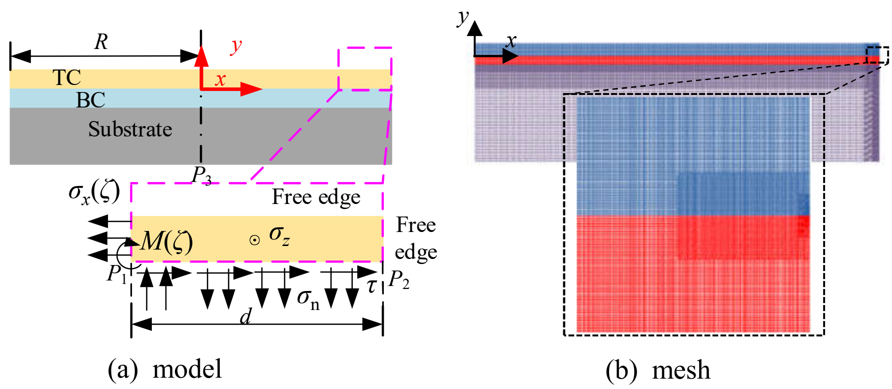


**Figure 3.** Schematic illustration of the coordinate system used in the analysis of thermal stress in the disk with TBC: (**a**) force analysis of the TC layer near the free edge; (**b**) FEM meshes of the TBC-substrate system and the refined meshes near the edge.

The shear stress $\tau$ and the normal stress $\sigma_\mathrm{n}$ are functions of the radial stress $\sigma_x$. A positive value of $\sigma_\mathrm{n}$ indicates the tendency for the coating to peel off the substrate. A simple analytical model is proposed for solving the radial stress $\sigma_x$ acting in the inner portion of the elastic multilayer due to thermal mismatch. The stress in the disk is similar to that of the unrestrained multilayer plate. Referring to Suhir [20], the strain at the interface can be expressed as Equation (5),

$$\begin{cases} \varepsilon_{x,i-1}^{+} = \varepsilon_{i-1}^{\mathrm{t}} + \lambda_{i-1}F_{i-1} + \frac{H_{i-1}}{2\rho} \\ \varepsilon_{x,i}^{-} = \varepsilon_{i}^{\mathrm{t}} + \lambda_{i}F_{i} - \frac{H_{i}}{2\rho} \end{cases} \tag{5}$$

where $\varepsilon_{x,i-1}^{+}$ and $\varepsilon_{x,i}^{-}$ refer to the strains of the upper side of the $(i-1)$th layer and the lower side of the $i$th layer ($i > 1$). The superscript 't' refers to thermal strain. $F$ is the total force of the radial stress across the cross section. Notably, $F$ is not actually a force, since the dimension of $F$ is N/mm. $\lambda$ is the coefficient of axial compliance and relates to the elastic modulus $E$ as well as Poisson's ratio $\nu$. The expression of $\lambda$ is shown in Equation (6) [20]. The thickness of the $i$th layer is $H_i$. Assuming that $\rho$ is the radius of curvature of the system, the strain induced by bending can be expressed as $H_i/(2\rho)$ [20].

$$\lambda = \frac{1-v}{EH} \tag{6}$$

Using the condition $\varepsilon_{x,i-1}^{+} = \varepsilon_{x,i}^{-}$ yields [20]:

$$-\lambda_i F_i + \lambda_{i-1} F_{i-1} + \frac{H_{i-1} + H_i}{2\rho} = \varepsilon_i^{\mathrm{t}} - \varepsilon_{i-1}^{\mathrm{t}} \tag{7}$$

Assuming the system consists of $m$ layers, there would be $m-1$ equations in the form of Equation (6). By summing the equations from $i = 1$ to $i = j$, then [20]:

$$F_j = \frac{1}{\lambda_j}\left(\lambda_1 F_1 - \varepsilon_j^{\mathrm{t}} + \varepsilon_1^{\mathrm{t}} + \frac{a_j}{\rho}\right) \tag{8}$$

where [20]:

$$a_j = \sum_{i=1}^{j} H_i - \frac{H_1 + H_j}{2} \tag{9}$$

Summing Equation (8) from $j = 1$ to $j = m$ yields [20]:

$$\sum_{i=1}^{m} \frac{1}{\lambda_i}(\lambda_1 F_1) - \sum_{i=1}^{m} \frac{\varepsilon_i^{\mathrm{t}} - \varepsilon_1^{\mathrm{t}}}{\lambda_i} + \frac{1}{\rho}\sum_{i=1}^{m} \frac{a_i}{\lambda_i} = 0 \tag{10}$$

The total radial force in the substrate (the first layer) can be expressed as [20]:

$$F_1 = \frac{\sum_{i=1}^{m} \frac{\varepsilon_i^{\mathrm{t}} - \varepsilon_1^{\mathrm{t}}}{\lambda_i} - \frac{1}{\rho}\sum_{i=1}^{m} \frac{a_i}{\lambda_i}}{\lambda_1 \sum_{i=1}^{m} \frac{1}{\lambda_i}} \tag{11}$$

Suhir [20] suggested the assumption that the multilayer structure is on a thick substrate. In the TBC system, the assumption would be invalid since the thickness of the substrate may be close to the sum of the thickness of other layers. To obtain a more accurate analytical solution to radial stress, this study considers the equilibrium equation of moment as:

$$\sum_{i=1}^{m} F_i\left(\sum_{j=1}^{i-1} H_j + \frac{H_i}{2}\right) + \sum_{i=1}^{m} \frac{E_i H_i^3}{12\rho(1 - v_i)} = 0 \tag{12}$$

According to Equations (11) and (12), the total force in the radial direction $F_i$ of each layer can be determined. The radial stress in each layer can be calculated by:

$$\sigma_i^{+} = \frac{F_i}{H_i} + \frac{E_i H_i}{2\rho(1 - v_i)} \tag{13}$$

$$\sigma_i^{-} = \frac{F_i}{H_i} - \frac{E_i H_i}{2\rho(1 - v_i)} \tag{14}$$

The superscript '+' indicates the upper side of the layer, and the superscript '−' indicates the lower side.

The original state image of TBC in Figure 2 shows that the TBC system is a three-layer system, while after oxidation in an elevated temperature environment, the TBC system is a four-layer system. The system without the TGO layer is studied in this section since the simpler model is sufficient to explain the nature of the thermal mismatch stress. The geometric parameters of each layer are listed in Table 2. The mechanical properties of the coating–substrate system for validation are listed in Table 3. Since the TGO will be studied in the following sections, the mechanical properties of TGO are also listed in Table 3. The analytical solution is validated by the FEM, and the results are listed in Table 4. The finite element meshes generated for FEM analysis are shown in Figure 3b. An axisymmetric linear elastic finite element analysis was performed using 4-node axisymmetric elements. The constraint in the $y$-direction is only set at point $P_3$ in Figure 3a, and no external force acts on the system. The $\Delta T$ used for validation is 100 °C. For simplification, the assumption of linear elasticity and static analysis is used.

The comparison of the analytical and FEM results ($\sigma_{x,\mathrm{A}}$ and $\sigma_{x,\mathrm{FEM}}$) for the calculated radial stress in the inner portion of the elastic multilayer structure are in excellent agreement. This validates the accuracy of the analytical model proposed previously. A contour map of the radial stress is shown in Figure 4, which illustrates that the radial stress away from the free edge changes only very slightly along the radial direction. As shown by Equations (13) and (14), the radial stress linearly changes with the layer thickness. For half-infinite plane, Equation (1) can be transformed into Equation (15). For the disk, Equation (15) could be used for estimating. Equation (4) can be transformed into Equation (16).

$$\int_0^R \tau(x)\mathrm{d}x = F_i \tag{15}$$

$$\int_0^R \sigma_\mathrm{n}(x)x^2\mathrm{d}x = -\int_0^R \sigma_\mathrm{n}(x)x(R-x)\mathrm{d}x \tag{16}$$

**Table 2.** Geometry of the model.

| Geometric Parameters | Value |
|---|---|
| Diameter of the disk $D$/mm | 25 |
| Thickness of the substrate $H_{\mathrm{sub}}$/mm | 3 |
| Thickness of the TC $H_{\mathrm{TC}}$/mm | 0.4 |
| Thickness of the BC $H_{\mathrm{BC}}$/mm | 0.25 |

**Table 3.** Mechanical properties of the coating–substrate system.

| Material \ Properties | $E$/GPa | $\nu$ | $\alpha/(10^{-6}/°\mathrm{C})$ |
|---|---|---|---|
| YSZ (TC) [40] | 70.0 | 0.20 | 11.01 |
| MCrAlY (BC) [40] | 137.9 | 0.27 | 15.37 |
| $Al_2O_3$ (TGO) [40] | 386.0 | 0.257 | 8.90 |
| GTD111 (Substrate) [41] | 110.0 | 0.30 | 13.70 |

**Table 4.** Calculated radial stress in the inner portion of the elastic multilayer due to thermal mismatch for $\Delta T$ = 100 °C.

| Location \ Results | $\sigma_{x,\mathrm{A}}$/MPa | $\sigma_{x,\mathrm{FEM}}$/MPa | $\frac{(\sigma_{x,\mathrm{A}}-\sigma_{x,\mathrm{FEM}})}{\sigma_{x,\mathrm{FEM}}}$ |
|---|---|---|---|
| TC (upper side) | 21.82 | 21.80 | 0.09% |
| TC (lower side) | 22.13 | 22.11 | 0.09% |
| BC (upper side) | −34.59 | −34.63 | −0.12% |
| BC (lower side) | −34.16 | −34.22 | −0.18% |
| Substrate (upper side) | −2.18 | −2.20 | −0.91% |
| Substrate (lower side) | 2.05 | 1.97 | 4.06% |

While cooling from 1100 °C, the failure occurred. As shown in Figure 5, the TC layer spalled from the rest part of the specimen, while the bondcoat still adhered to the substrate. The experimental result reveals that the interfacial stresses between the TC and the BC are the mean cause of the thermal mismatch failure. The interfacial normal stress and the interfacial shear stress are the emphasis of this paper. Suhir [20,21] presented an analytical formula relating shear stress $\tau$ and interfacial normal stress $\sigma_\mathrm{n}$. However, those formulas do not apply to systems with thick coatings since the maximum shear stress is not at $x = R$. In fact, to meet the conditions of the free edge, $\tau(R) = 0$ and $\sigma(R) = 0$. With finer meshes, the maximum shear stress clearly occurs at $x = R - \delta$, and the value of $\delta$ is related to the geometric and material variations of the coating–substrate system. From the equations above, it is clear that the material and geometric characteristics affecting the interfacial stress should be the CTE, elastic modulus, Poisson's ratio, and thickness of each layer. Since the analytical model could not describe the stress state near the free edge, the FEM is used to analyze the effects of these variations of the coating–substrate system.

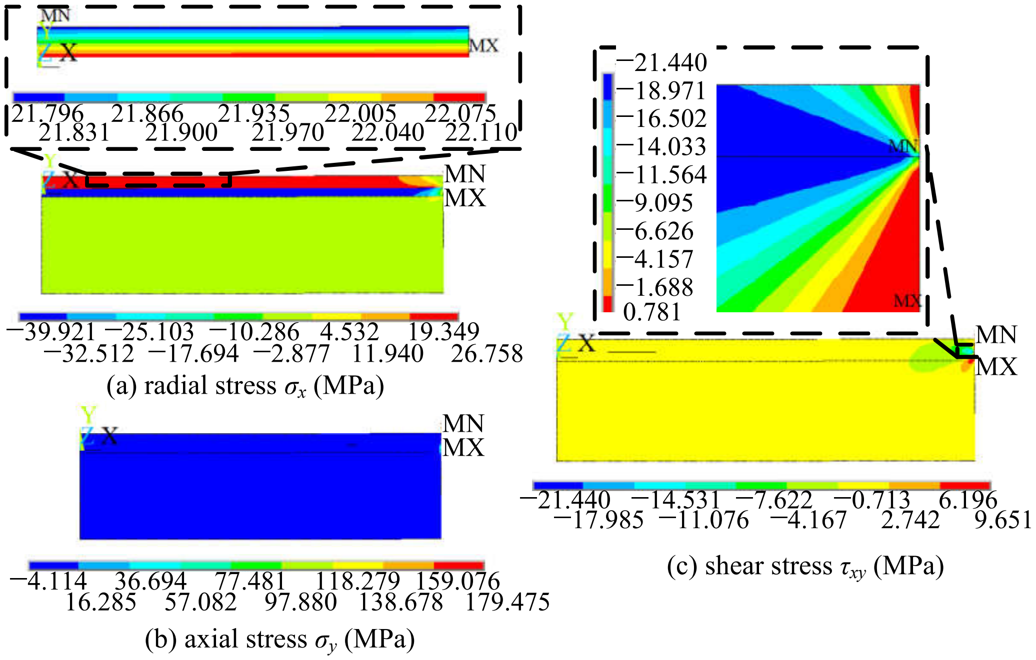


**Figure 4.** The distribution of thermal mismatch stress of the disk with TBC for $\Delta T$ = 100 °C.

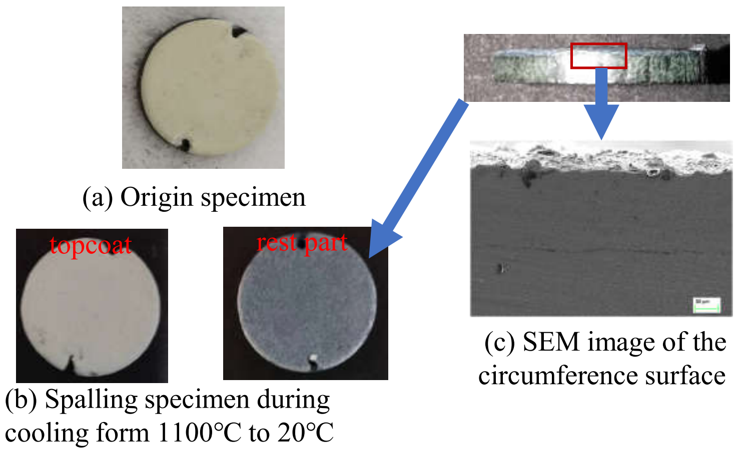


**Figure 5.** The separation of TC from the disk-shaped specimen while cooling from 1100 °C to 20 °C.

Notably, the finite element solutions for $\tau$ and $\sigma_n$ in the edge region have errors, but finer meshes could reduce these errors. Since the size of the mesh has a significant effect on the numerical modeling results, finer and more regular meshes are suggested to be adopted near the edge, as shown in Figure 3b. The minimum length of the mesh near the edge is $1 \times 10^{-5}$ µm. As the length of the mesh near the edge decreases from $4 \times 10^{-5}$ µm to $1 \times 10^{-5}$ µm, the maximum interfacial shear stress rises by only 1.36%. A study on mesh sensitivity reveals that the fineness of the mesh near the edge is sufficient to obtain a relatively accurate stress value.

To better understand the interfacial shear and normal stresses, the stresses between the TC and BC at each point on the interface are plotted versus the distance $d$ from the point to the edge in Figure 6.

As mentioned above, the interfacial shear stress at the free edge is zero. As the distance from the point to the edge increases, the shear stress rapidly rises to the maximum magnitude at point $A_3$ in Figure 6 and then decreases gradually to zero at point $A_2$ in Figure 6. Then, the shear stress remains zero. The interfacial normal stress also gradually decreases to zero in the inner portion of the disk. Unlike the shear stress, the interfacial normal stress decreases to zero, and the tensile stress becomes compressive at point $A_4$ in Figure 6. Then, the compressive normal stress decreases, reaches zero again at point $A_1$ in Figure 6, and remains zero. Comparing the distance from the edge to point $A_1$ with the distance from the edge to point $A_2$ in Figure 6, the interfacial normal stress requires a much shorter distance to reach zero than the interfacial shear stress. When the distance from one point on the interface to the edge exceeds the distance from point $A_2$ to the edge, the interfacial stress and radial stress barely not change along the radial direction [21]. That is, the mesh in the inner potion could be much coarser than the mesh near the edge. When the coating–substrate system becomes more complex, the submodel method is valid for the stress analysis near the free edge.

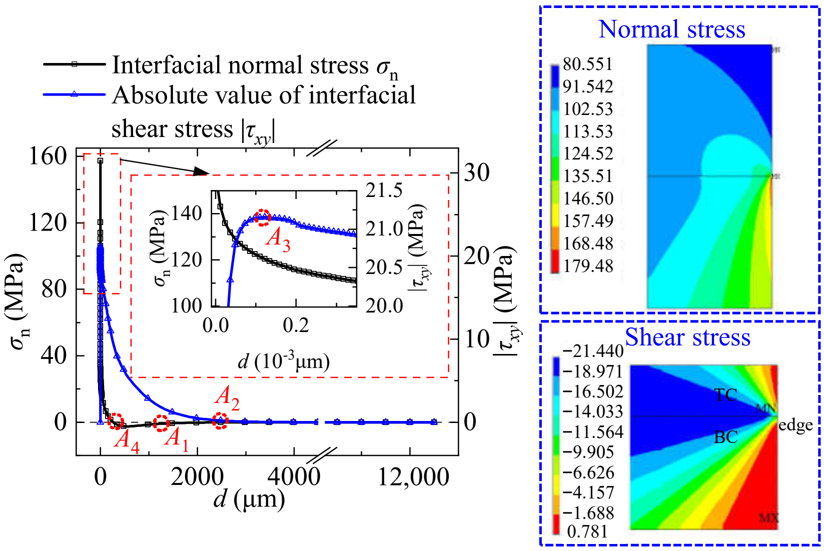


**Figure 6.** The interfacial normal stress $\sigma_n$ and the absolute value of the interfacial shear stress $\tau_{xy}$ between the TC and BC for $\Delta T$ = 100 °C.

The interfacial stress profile illustrates that it is difficult to find a simple function that shows a trend similar to the curve. The FEM is chosen to study how the geometric and material variations mentioned above affect the profile of the interfacial stress. The maximum values of the interfacial normal and shear stress, as well as the distance from the edge to the location where the stress reaches the maximum magnitude, are important factors in depicting the stress curve. The other factors are the distances $d$ corresponding to points $A_1$ and $A_2$ marked in Figure 6.

Another issue that must be solved is that it is difficult to obtain the interfacial stress at the edge due to the limits of the FEM. The result of the calculation of the interfacial stress is unstable as it changes with changes in the mesh size at the edge. Therefore, the magnitude of the interfacial stress cannot be used to describe the damage directly. The integral value $\psi_1$ shown in Equation (17) is proposed to replace the magnitude of the interfacial normal stress. The integral value $\psi_2$ shown in Equation (18) is proposed to replace the magnitude of the interfacial shear stress.

$$\psi_1 = \int_{R-d_{A_2}}^{R} \sigma_n(x)x(R-x)dx \tag{17}$$

$$\psi_2 = \left| \int_{R-d_{A_2}}^{R} \tau(x)xdx \right| \tag{18}$$

where $d_{A_2}$ is the distance from the edge to point $A_2$ (marked in Figure 6) where the shear stress approaches zero and changes very little. The variation $x$ is defined as the radial coordinate. The integral value $\psi_1$ is a sum of the moment in essential and the integral value $\psi_2$ is a sum of the shear force. The integral value is then divided by unit angle d$\theta$. The multiplier d$\theta$ in the integral is omitted. While the study object is a plate, the $x$ in the integral is also omitted. Then, considering the force equilibrium equation (Equation (1)) and the moment equilibrium equation (Equation (4)), the magnitudes of $\psi_1$ and $\psi_2$ are stable since the stress magnitude in the inner portion of the FEM model is generally stable. Two models with meshes of different finenesses are used to validate the stability of the integral parameters. The results shown in Table 5 indicate that the integral value is more stable compared with the computed stress value. Realistically, in the stress analysis of complex components, the length of the mesh could not be as small as $1 \times 10^{-5}$ μm. The integral value may be a suitable parameter with which to evaluate the damage and predict the service life of the component.

**Table 5.** Calculated results of the model in Section 2 with different meshes for $\Delta T$ = −100 °C.

| The Length of the Mesh Near the Edge/μm | $\sigma_n$/MPa | $\tau_{xy}$/MPa | $\psi_1$/N·mm | $\psi_2$/N |
|---|---|---|---|---|
| $1 \times 10^{-5}$ | −157.246 | −21.15 | 21.614 | 108.597 |
| 0.2 | −69.508 | −18.52 | 21.487 | 108.356 |
| $\frac{(X_{\text{line2}} - X_{\text{line 1}})}{X_{\text{line 1}}}$ | −55.797% | −12.43% | −0.588% | −0.222% |

## 3. Paramater Analysis

The equations in Section 2 illustrate that the thickness, elastic modulus, Poisson's ratio, and thermal strain of each layer have significant effects on the interfacial stress between layers. It is unnecessary to study every variation of the system. Therefore, the geometric and material variations that differ in the deposition or spraying process and in service are chosen as the study objects. The first is the thermal mismatch strain, which may change during different service conditions. Meanwhile, the thermal mismatch strain is also related to the CTE and the stress-free temperature of each material [42]. The thickness of each layer is also different in various coating–substrate systems. For example, the coating used in a stationary gas turbine has a thicker TC layer than the coating used in an aero-engine; The substrate is also thicker. Therefore, the thickness of the TC layer is studied below. The oxidation of MCrAlY is significant when the TBC system is in service, and the TGO affects the spalling of the TBC system. Therefore, the TGO thickness is another variation to be considered. The elastic modulus and Poisson's ratio of YSZ are the last two parameters to be studied since the two material parameters vary greatly from one kind of preparation process to another. The commonly used preparation processes are air plasma spraying (APS) and electron beam physical vapor deposition (EB-PVD). The elastic modulus of YSZ even changes due to sintering in service [43].

### *3.1. Effects of Thermal Mismatch Strain*

The effects of thermal mismatch strain are analyzed in this section. The thermal mismatch strain can be expressed with Equation (19).

$$\Delta\varepsilon_i^{\mathrm{t}} = \varepsilon_i^{\mathrm{t}} - \varepsilon_1^{\mathrm{t}} = \alpha_i \Delta T_i - \alpha_1 \Delta T_1 \tag{19}$$

If the stress-free temperature $T_{\mathrm{sf}}$ of each material is the same and the temperature distribution of the coating–substrate system is uniform, then the thermal mismatch strain is proportional to the temperature difference $\Delta T$. The interfacial stresses between the TC and BC in the cases when $\Delta T$ is equal to −100 °C, 100 °C, 300 °C, 500 °C, and 800 °C are plotted in Figures 7 and 8.

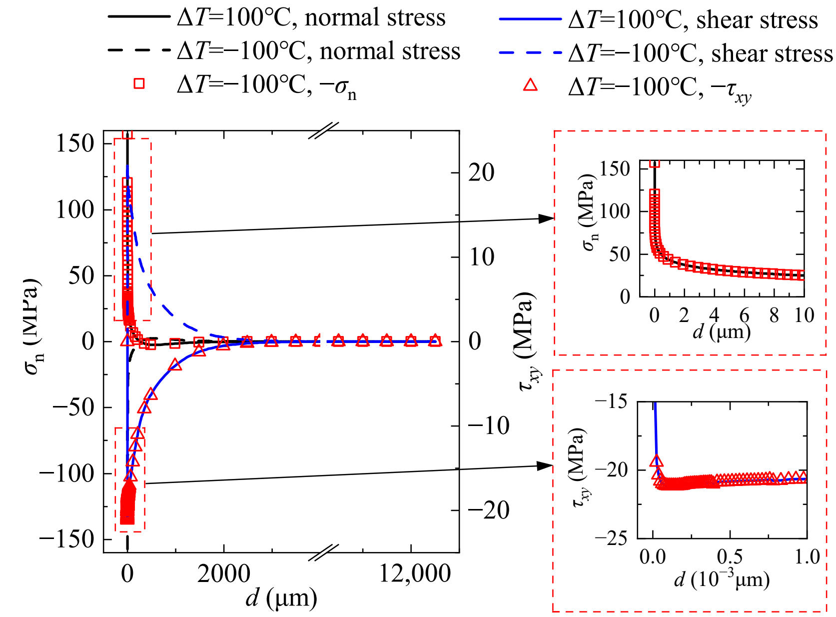


**Figure 7.** The distributions of the interfacial normal stress $\sigma_n$ and the interfacial shear stress $\tau_{xy}$ for $\Delta T$ = 100 °C and $\Delta T$ = −100 °C.

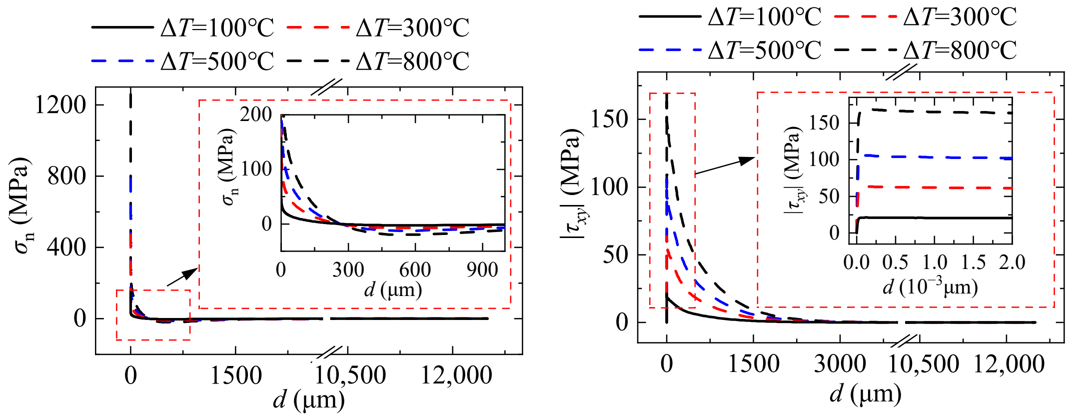


(**a**) (**b**)

**Figure 8.** The interfacial normal stress $\sigma_n$ and the absolute value of the interfacial shear stress $\tau_{xy}$ between TC and BC for different $\Delta T$: (**a**) interfacial normal stress $\sigma_n$; (**b**) absolute value of the interfacial shear stress $\tau_{xy}$.

The normal and shear stress concentrations occurring at the interface close to the free edge are proportional to the temperature difference. In Figure 8a, the interfacial normal stress reverses for the first time at the same point in all cases. In Figure 8b, the interfacial shear stress also reaches zero at the same point in all cases. According to Equations (8), (11) and (12), the virtual force $F_i$ is proportional to $\Delta T$. Combining Figure 8 and Equations (15) and (16), it can be inferred that the shape of the curve corresponding to $\tau$ and $\sigma_n$ should not be affected by $\Delta T$.

However, this conclusion is based on the linear elastic assumption. Additionally, while the temperature difference of each layer is not the same, the distributions of interfacial normal and shear stress would be more complex. The thermal strain difference between two materials in the TBC system is determined by the preparing temperature and the working temperature. The effects associated with the preparing temperature and the working temperature will be discussed in Section 3.4.

### *3.2. Effects of Geometric Parameters*

The effects of the TC thickness $H_{TC}$ are considered since the thickness varies in different thermal protection structures. The interfacial normal and shear stresses between the TC and BC are plotted in Figures 9a and 10a. The thickness of TCs used on gas turbine blades varies from 100 μm to 500 μm. However, to magnify the effects of TC thickness, the maximum thickness is chosen as 1500 μm, i.e., half of the thickness of the substrate $H_{sub}$. The temperature difference is set to 100 °C.

As the thickness of the TC increases from 100 μm to 500 μm, the interfacial normal stress at the edge rises by 13.60%; as the thickness of the TC increases from 100 μm to 1500 μm, the interfacial normal stress at the edge rises by 22.90%. Unlike normal stress, the maximum interfacial shear stress changes little with the TC thickness. The percentage of the variation is only 5.47% as the thickness of the TC increases from 100 μm to 1500 μm.

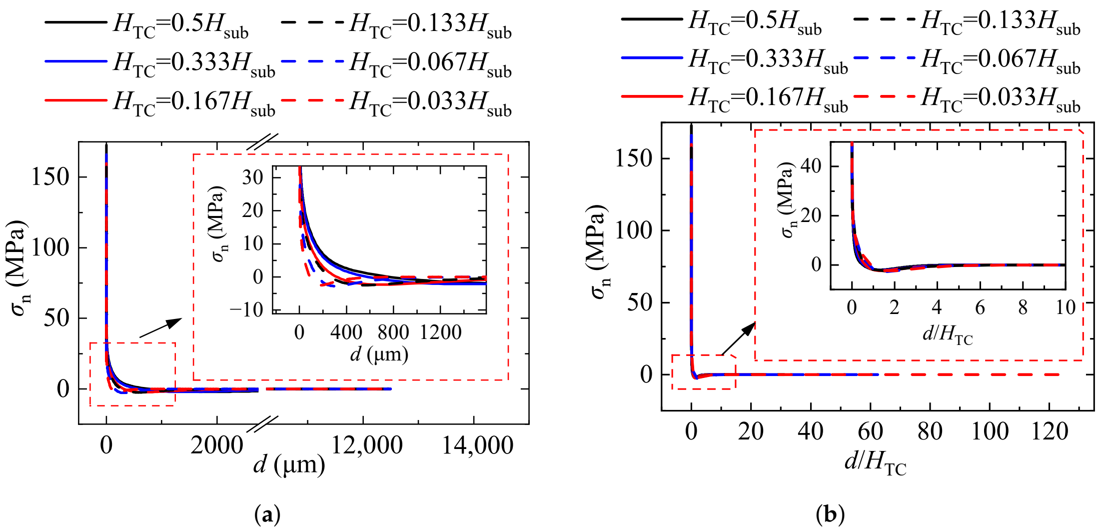


**Figure 9.** Interfacial normal stress $\sigma_n$ between the TC and BC for thicknesses of the TC: (**a**) interfacial normal stress $\sigma_n$ versus distance $d$ from the point to the edge; (**b**) interfacial normal stress $\sigma_n$ versus the ratio of the distance from the point to the edge to the TC thickness ($d/H_{TC}$).

However, there are significant changes in the distribution of interfacial stress. The radial distance between the point from where the interfacial shear stress remains zero, i.e., point $A_2$, and the edge varies from approximately 500 μm to 5000 μm. The range of the normal stress is not as large as that of the shear stress, but the trend is similar. If a similar nondimensional stress profile is obtained, then the region that may be affected by the free edge can be determined. As shown in Figures 9b and 10b, while the interfacial stress is plotted versus the ratio of the distance from the point to the edge to the TC thickness, the points where the stress reaches zero appear to be close to each other. That is, the ratio of the distance from the point to the edge to the TC thickness can be a representative nondimensional parameter used to describe the stress profiles of $\tau$ and $\sigma_n$ in the TBC system. The size of the submodel region can be determined from this nondimensional parameter.

The thickness of the TC is fixed at 400 μm, and the thickness of the BC is investigated at 100 μm, 200 μm, 400 μm, and 500 μm. Figure 11 shows that with increasing thickness of the BC from 100 μm to 500 μm, the maximum interfacial stress at the edge decreased by less than 1%. The material properties of the BC are similar to the properties of the substrate metal. Similar effects occur whether increasing the thickness of the BC or increasing the thickness of the substrate; a similar result is caused by decreasing the thickness of the TC.

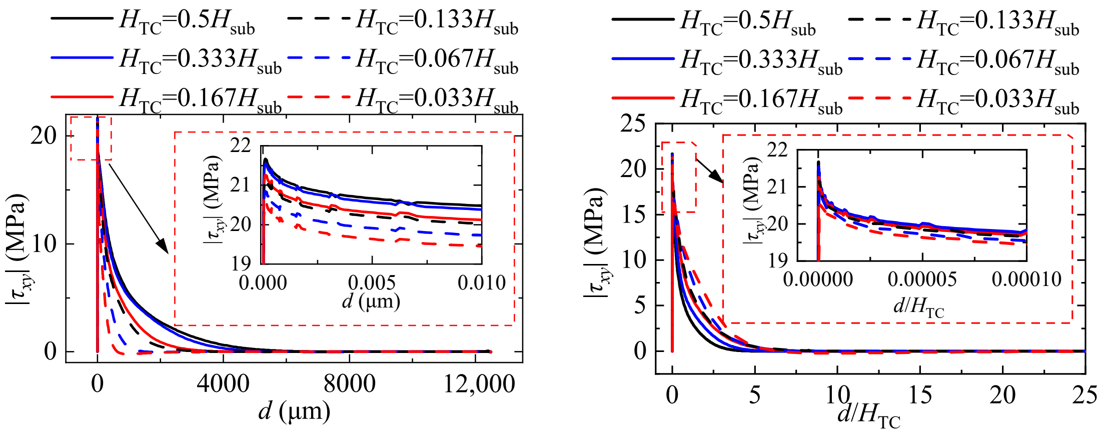


(**a**) (**b**)

**Figure 10.** The absolute value of the interfacial shear stress $\tau_{xy}$ between the TC and BC for thicknesses of the TC: (**a**) absolute value of the interfacial shear stress $\tau_{xy}$ versus distance $d$ from the point to the edge; (**b**) absolute value of the interfacial shear stress $\tau_{xy}$ versus the ratio of the distance from the point to the edge to the TC thickness ($d/H_{TC}$).

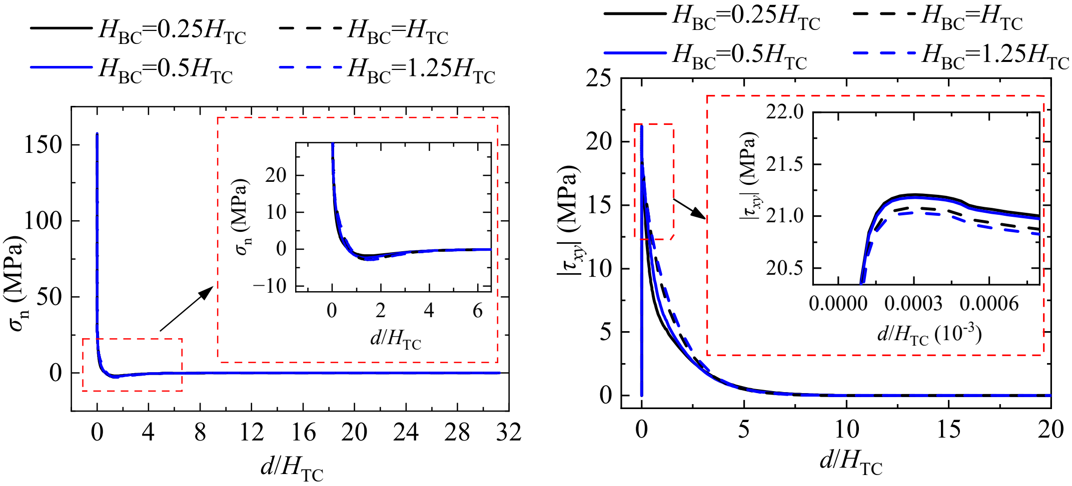


(**a**) (**b**)

**Figure 11.** The interfacial normal stress $\sigma_n$ and the absolute value of the interfacial shear stress $\tau_{xy}$ between the TC and the BC for different thicknesses of the BC: (**a**) interfacial normal stress $\sigma_n$; (**b**) absolute value of the interfacial shear stress $\tau_{xy}$.

The TGO layer, which is generated due to the oxidation of the BC, has quite different material properties from the other layers. The TGO consists of $Al_2O_3$ and other metal oxides. Compared with MCrAlY, it has a lower CTE and higher elastic modulus. The thickness of the TGO layer is a function of the heating time [44,45]. To study the effects of the TGO thickness on the interfacial stress, 1 μm, 3 μm, 5 μm, and 8 μm meshes in the BC layer near the TC layer in the reference model are set for the TGO layer. The meshes are refined near the edges and interfaces. The interfacial stresses on both sides of TGO are large. However, the picture and data from Energy Disperse Spectroscopy (EDS) (shown in Figure 12) indicate that the separation mainly occurs at the interface between TC and TGO. In Figure 12a, the color of the TGO is darkest because of the poor electrical conductivity, and in Figure 12b, the count per second (cps) of Al is high in the region of TGO. Also, the cps of Zr is high in the region of TC. This is due to the TC containing $ZrO_2$. The aluminium content is extremely low in the light-colored region in the EDS figure of the spalling part

(Figure 12c), while the aluminium content is high on the other side in Figure 12d. Thus, in this paper, the interfacial stresses at the interface between TC and TGO are discussed.

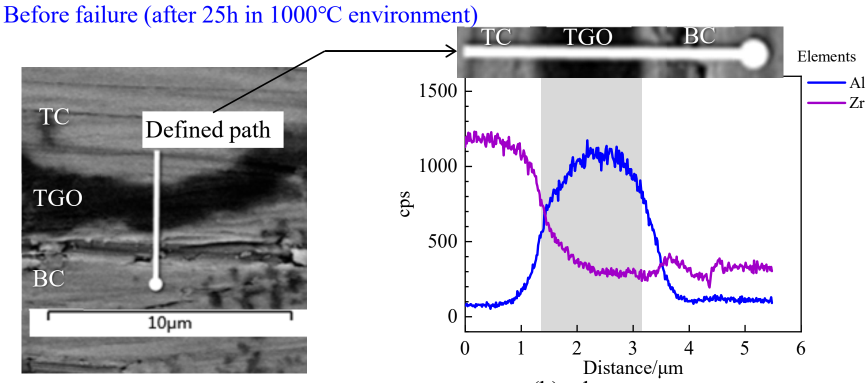


(a) SEM image for TGO layer (b) element content

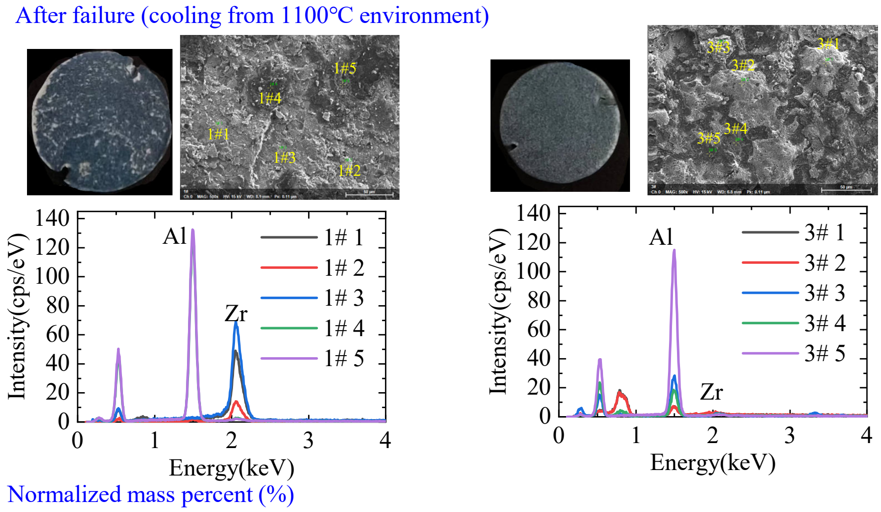


| Location | Al | Zr |
|---|---|---|
| 1# 1 | 0.27 | 99.73 |
| 1# 2 | 3.58 | 96.42 |
| 1# 3 | 0.23 | 99.77 |
| 1# 4 | 93.55 | 6.45 |
| 1# 5 | 95.06 | 4.49 |

(c) element content in each points on the spalling part

| Location | Al | Zr |
|---|---|---|
| 3# 1 | 53.69 | 46.31 |
| 3# 2 | 44.33 | 55.67 |
| 3# 3 | 81.80 | 18.20 |
| 3# 4 | 83.29 | 16.71 |
| 3# 5 | 96.50 | 3.50 |

(d) element content in each points on the rest part

**Figure 12.** EDS figures/data of samples before and after failure.

The results are shown in Figure 13. The TGO layer is extremely thin compared with the other layers. The presence of the TGO hardly affects the radial and hoop stresses in the inner portion far from the free edge. However, Figure 13 demonstrates that the presence of the TGO layer greatly alters the distribution of interfacial stress. The CTE of the TGO is smaller than the CTE of the TC. As a result, the interfacial normal stress and shear stress close to the free edge are opposite in sign compared with the case without TGO. The change of sign explains the spalling of the topcoat during the cooling period. Away from the edge, the interfacial shear stress decreases to zero along the radial direction but does not remain zero. The interfacial shear stress then reverses and increases to the second maximum magnitude and finally returns to zero. This is different from the case without TGO. The interfacial normal stress has the same trend as in the case without TGO, but the maximum absolute value of the second peak increases. The maximum absolute values of the interfacial shear and normal stresses increase with increasing TGO thickness, while the maximum absolute value of the second peak decreases with increasing TGO thickness.

Considering that the presence of TGO changes the distributions of interfacial stress, the effects of the TC thickness on the interfacial stress of the model with a 3 μm TGO layer are also analyzed. The results are shown in Figure 14. With increasing TC thickness, the interfacial stress near the edge between the TC and TGO decreases. On the other hand, the magnitude of the stress in the inner portion is larger.

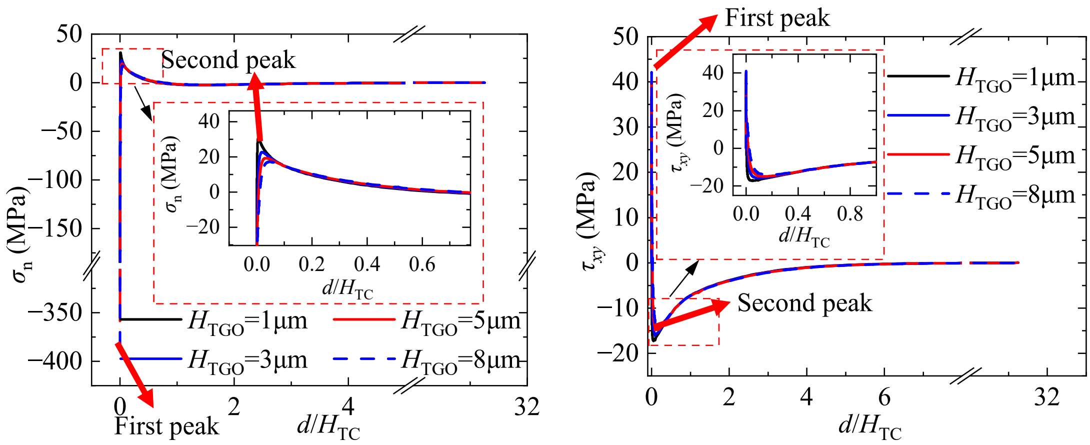


(**a**) (**b**)

**Figure 13.** The interfacial normal stress $\sigma_n$ and interfacial shear stress $\tau_{xy}$ between the TC and the TGO for different thicknesses of the TGO layer: (**a**) interfacial normal stress $\sigma_n$; (**b**) the interfacial shear stress $\tau_{xy}$.

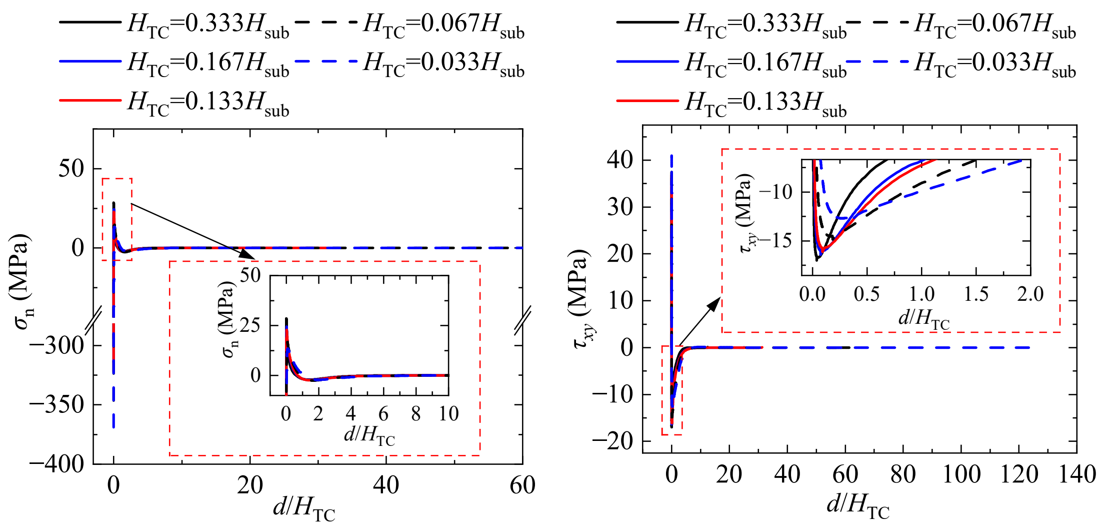


(**a**) (**b**)

**Figure 14.** The interfacial normal stress $\sigma_n$ and interfacial shear stress $\tau_{xy}$ between the TC and the TGO for different thicknesses of the TC with a 3 μm TGO layer: (**a**) interfacial normal stress $\sigma_n$; (**b**) the interfacial shear stress $\tau_{xy}$.

### *3.3. Effects of Material Properties*

For a variable elastic modulus and Poisson's ratio of the TC, the interfacial stress versus the ratio of the distance $d$ from the point to the edge to the TC thickness is plotted in Figures 15 and 16. The temperature difference is set to 100 °C . The variations in the material properties of the TC affect not only the magnitude of the interfacial stress but also the distribution of the stress.

The effects of the mechanical properties of the coating–substrate system on the stress distribution are studied by analyzing how three specific points on the stress curve and the maximum change in shear stress with respect to changes in the elastic modulus and Poisson's ratio of the TC.

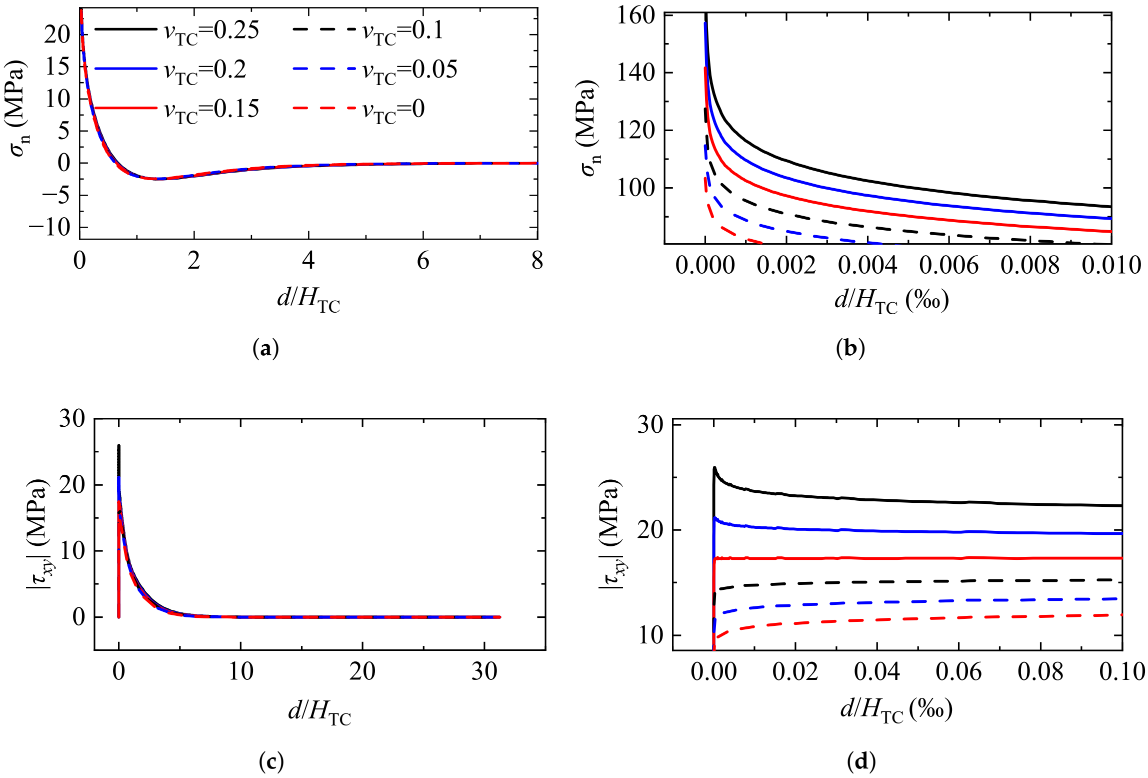


**Figure 15.** The distribution of interfacial normal stress $\sigma_{\mathrm{n}}$ and the absolute value of the interfacial shear stress $\tau_{xy}$ for different values of $\nu_{\mathrm{TC}}$ when $E_{\mathrm{TC}}$ = 70 GPa: (**a**) the interfacial normal stress $\sigma_{\mathrm{n}}$; (**b**) the interfacial normal stress $\sigma_{\mathrm{n}}$, near the edge, (**c**) the absolute value of interfacial shear stress $\tau_{xy}$; (**d**) the absolute value of interfacial shear stress $\tau_{xy}$, near the edge.

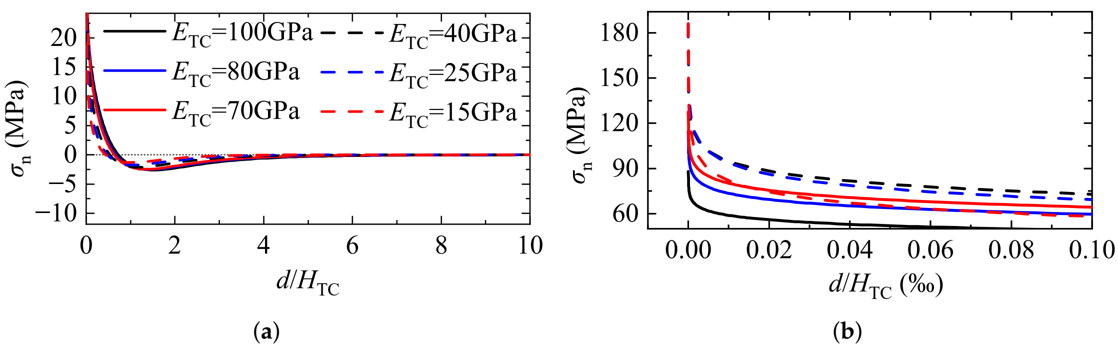


**Figure 16.** *Cont.*

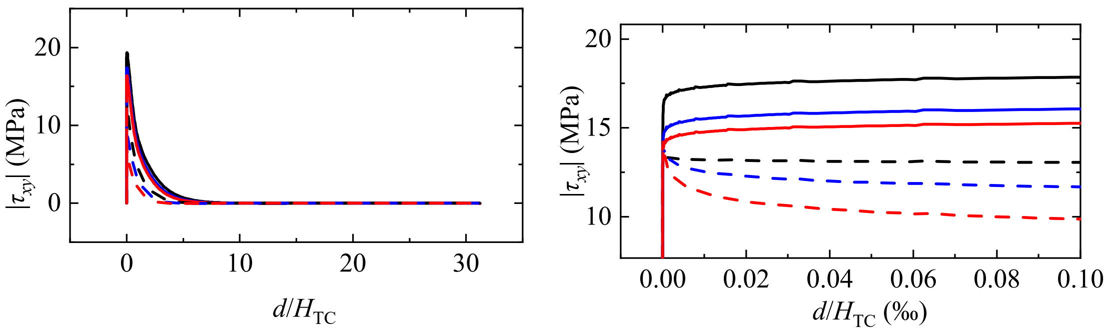


(**c**) (**d**)

**Figure 16.** The distribution of interfacial normal stress $\sigma_n$ and the absolute value of the interfacial shear stress $\tau_{xy}$ for different values of $E_{TC}$ when $\nu_{TC} = 0.1$: (**a**) the interfacial normal stress $\sigma_n$; (**b**) the interfacial normal stress $\sigma_n$, near the edge, (**c**) the absolute value of interfacial shear stress $\tau_{xy}$; (**d**) the absolute value of interfacial shear stress $\tau_{xy}$, near the edge.

Point $A_2$ (marked in Figure 6) represents the location where the interfacial shear stress reaches zero and remains unchanged. Figure 17 indicates that as the elastic modulus and Poisson's ratio increase, the region affected by the edge effect becomes larger. Point $A_1$ (marked in Figure 6), which represents the location where the interfacial normal stress reaches zero and remains unchanged, is always closer to the free edge than point $A_2$. The ratio of the distance from the edge to the point at which the normal stress reaches zero for the first time (defined as point $A_4$, marked in Figure 6) to the TC thickness is plotted in Figure 18. The trend is the same as that in Figure 17. As the elastic modulus and Poisson's ratio increase, the point where the normal stress reaches zero for the first time moves away from the free edge.

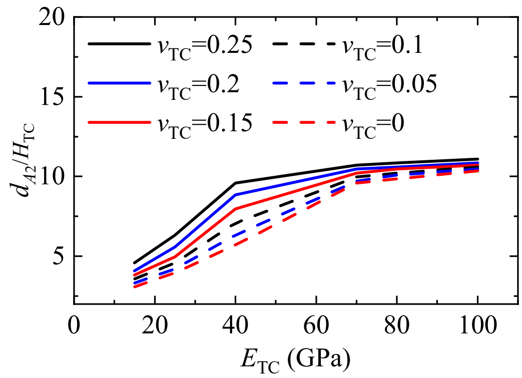


**Figure 17.** The ratio of the distance from the edge to point $A_2$ where the shear stress reaches zero and remains unchanged to the thickness of the TC ($d_{A_2}/H_{TC}$) versus the elastic modulus of the TC ($E_{TC}$).

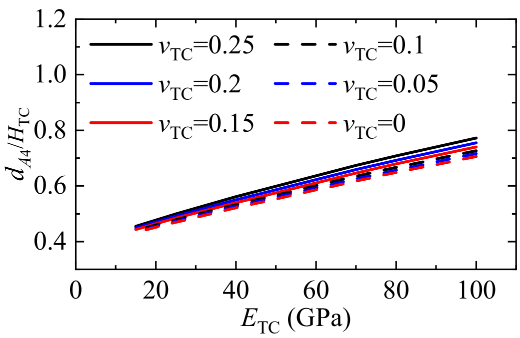


**Figure 18.** The ratio of the distance from the edge to point $A_4$ where the normal stress reaches zero for the first time to the thickness of the TC ($d_{A_4}/H_{TC}$) versus the elastic modulus of the TC ($E_{TC}$).

Point $A_3$ (marked in Figure 6) represents the location where the interfacial shear stress reaches the maximum magnitude. Figures 19 and 20 illustrate that the maximum shear stress increases with the elastic modulus and Poisson's ratio. The distance from the edge to where the shear stress reaches a maximum magnitude increases with increasing elastic modulus but decreases with increasing Poisson's ratio.

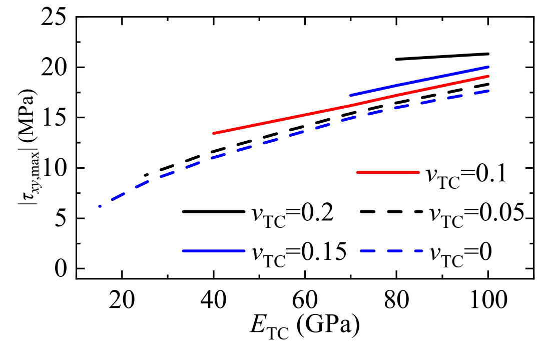


**Figure 19.** Maximum absolute value of the interfacial shear stress $\tau_{xy}$ versus the elastic modulus of the TC ($E_{TC}$).

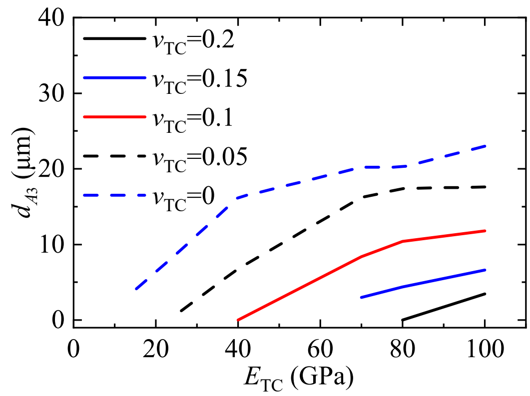


**Figure 20.** The distance from the edge to point $A_3$ where the shear stress reaches the maximum magnitude ($d_{A_3}$) versus the elastic modulus of the TC ($E_{TC}$).

### *3.4. The Preparing Temperature and the Growth Strain of TGO*

#### 3.4.1. The Numerical Analysis

The analyses above are on the conditions that the 'stress-free temperatures' $T_{sf}$ of all the materials in TBC systems are the same, whereas in turbine blades this is generally not so. While preparing the TBC on the substrate by APS, the coating powders in elevated temperature (e.g., $T_c$ = 2000 °C) inject from the spray gun onto the substrate or bondcoat. The substrate or the bondcoat is preheated to preheating temperature (e.g., $T_s$ = 100 °C). Using the heat quantity balance, the balance temperature $T_b$ of the TBC system can be obtained for different combinations of $T_c$ and $T_s$. At $T_b$, the coating solidifies and adheres to the substrate without any thermal mismatch stress in the systems. In contrast with TC and BC, the TGO layer is formed in a more harsh thermal environment (e.g., $T_w$ = 1100 °C).

To simplify the computation procedure, the 'stress-free temperature' of YSZ and MCrAlY is assumed to be the balance temperature $T_b$, and the 'stress-free temperature' of $Al_2O_3$ is assumed to be the working temperature $T_w$. At 'stress-free temperature', the thermal strain of YSZ, MCrAlY, and $Al_2O_3$ equals that of the substrate. Translate the temperature-thermal strain curve to where the thermal strain at 'stress-free temperature' of YSZ/MCrAlY/$Al_2O_3$ equals that of the substrate. Then, the 'reference temperature' at which the thermal strain of each material is zero can be obtained, i.e., the point where the curve intersects the horizontal axis. The assumption is that the slope of the temperature-thermal strain curve remains constant at the same temperature regardless of the reference temperature. When the $T_b$ is assumed to be 200 °C and the $T_w$ is assumed to be 1100 °C, combining the material parameters in Table 3, the reference temperature of YSZ, MCrAlY, and $Al_2O_3$ is −48.87 °C, 21.73 °C , and −593.26 °C , respectively. The translated temperature-thermal strain curves are plotted in Figure 21.

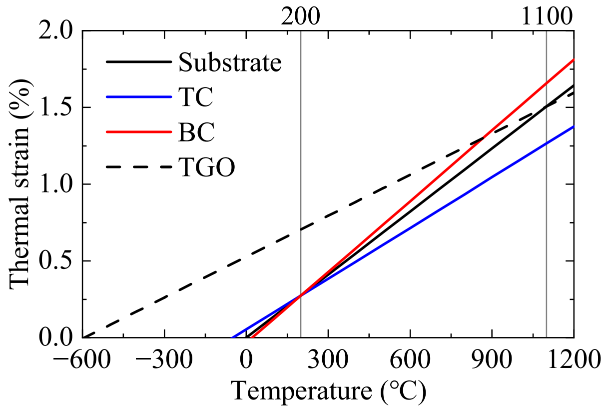


**Figure 21.** The illustration of the reference temperature.

In addition to the thermal strain, the TGO's lateral growth strain also leads to the strain mismatch stress in the TBC. According to Clark [46], the linear relationship between the rate of change of the TGO thickness $h_{TGO}$ and the growth strain $\varepsilon^G_{TGO}$ is expressed as

$$\dot{\varepsilon}^G_{TGO} = \beta \dot{h}_{TGO} \tag{20}$$

where $\beta$ is a constant and is inversed with the isothermal degradation test in Ref. [47] to be 125 $m^{-1}$. The TGO growth strain corresponding to the TGO thickness could be calculated when the growth curve of TGO is determined. The growth strain curve obtained from Ref. [47] is plotted in Figure 22.

Take into account the preparing temperature, working temperature, and the TGO growth strain, and then recalculate the strain mismatch interfacial stress in the disk-shaped model in Section 3.2. The strain mismatch stresses during cooling from 1100 °C to 20 °C are calculated by FEM. The interfacial normal and shear stresses of the model with 400 µm TC and 1/3/5/8 µm TGO are shown in Figure 23. Also, the effects of TC thickness are restudied. The interfacial normal and shear stresses for the model with 3 µm TGO and 100/200/400/500/1000 µm TC are shown in Figure 24.

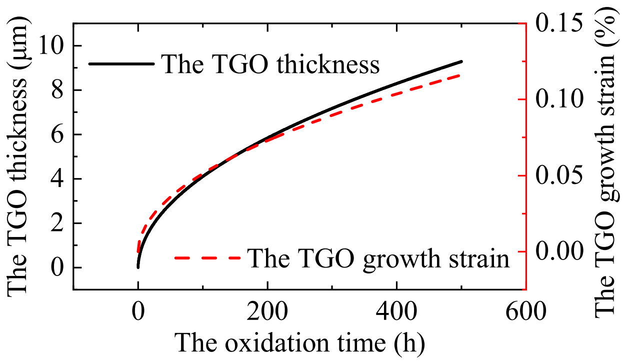


**Figure 22.** The thickness and growth strain of TGO versus the oxidation time.

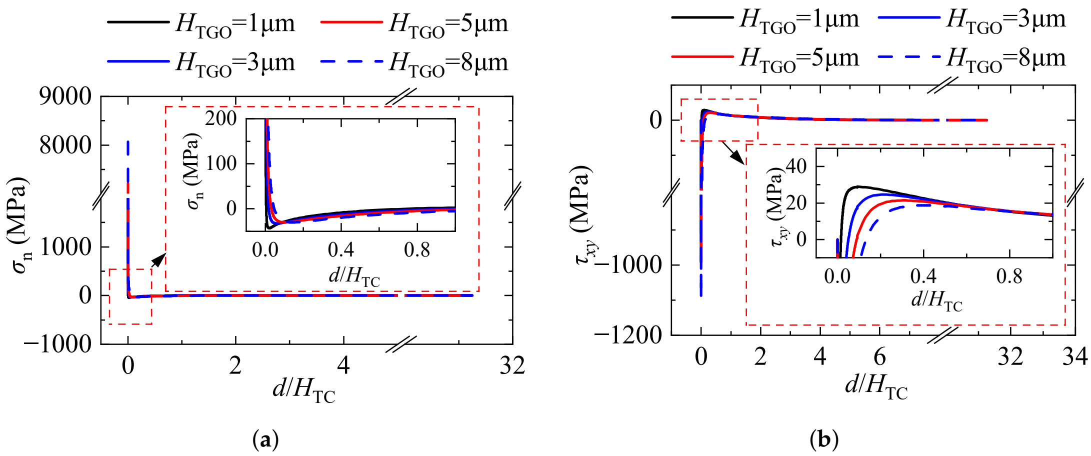


**Figure 23.** The interfacial normal stress $\sigma_n$ and interfacial shear stress $\tau_{xy}$ between the TC and the TGO for different thicknesses of the TGO layer considering the different reference temperatures and the TGO growth strain: (**a**) interfacial normal stress $\sigma_n$; (**b**) the interfacial shear stress $\tau_{xy}$.

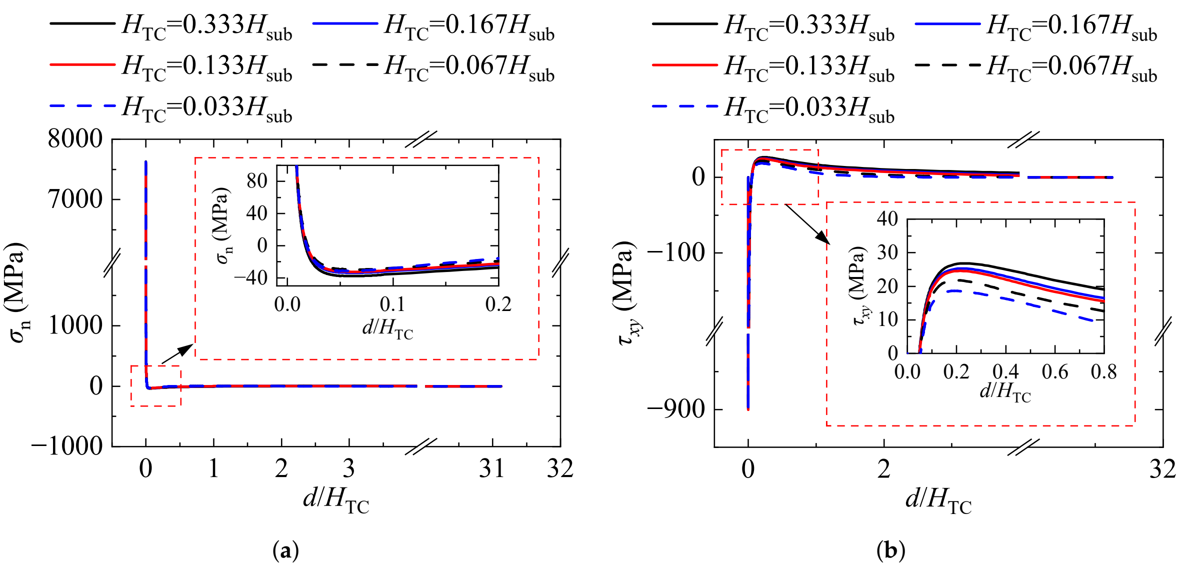


**Figure 24.** The interfacial normal stress $\sigma_n$ and interfacial shear stress $\tau_{xy}$ between the TC and the TGO for different thicknesses of the TC with a 3 μm TGO layer considering the different reference temperatures and the TGO growth strain: (**a**) interfacial normal stress $\sigma_n$; (**b**) the interfacial shear stress $\tau_{xy}$.

The distribution of the interfacial stress hereinabove is similar to the results of the model in Section 3.2 when the $\Delta T$ is negative. The maximum absolute values of the interfacial shear and normal stresses increase with increasing TGO thickness, while the maximum absolute value of the second peak decreases with increasing TGO thickness. With increasing TC thickness, the interfacial stress near the edge between the TC and TGO decreases, while the maximum absolute value of the second peak increases with increasing TGO thickness. Moreover, as the thickness of TC increases, the region affected by the edge effect becomes larger.

The stability of the integral value proposed in Section 2 is also validated below. The results shown in Table 6 indicate that the integral value is more stable compared with the computed stress value.

**Table 6.** Calculated results of the model in Section 3.4 with different meshes for $T$ = 20 °C, $H_{TC}$ = 400 μm and $H_{TGO}$ = 3 μm.

| The Length of the Mesh Near the Edge/μm | $\sigma_n$/MPa | $\tau_{xy}$/MPa | $\psi_1$/N·mm | $\psi_2$/N |
|---|---|---|---|---|
| $1 \times 10^{-5}$ | 6430.0 | −900.1 | 34.076 | 171.655 |
| 0.2 | 1044.1 | −374.3 | 34.076 | 172.325 |
| $\frac{(X_{line2} - X_{line\,1})}{X_{line\,1}}$ | −83.8% | −58.4% | <1‰ | 0.390% |

From the numerical calculation results above, whether with or without the TGO, the thickness of TC has a significant impact on the interfacial normal stress inside the TBC system. The thicker the TC, the larger the $\psi$ (as shown in Figure 25), which means the TBC system with thicker TC is more likely to fail during the cooling stage. To reach this conclusion, we carried out a temperature variation test with disk-shaped specimens with TC in different thicknesses.

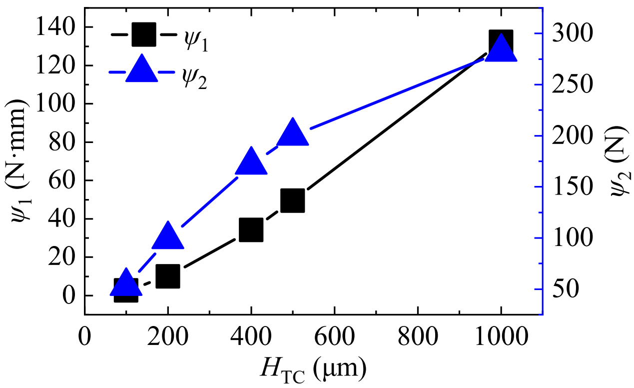


**Figure 25.** The $\psi_1$ and $\psi_2$ versus the thickness of TC when $H_{TGO}$ = 3 μm and $T$ = 20 °C.

3.4.2. Experimental Verification

Six disk-shaped Ni-based superalloy GTD111 was processed. The diameter of the specimens is 12 mm, and the thickness of GTD111 is 1.5 mm. A TBC was applied on the surface of the GTD111 sample. The TC was applied using air plasma spraying with 8% YSZ powder, and the BC was applied using the high-velocity oxygen fuel (HVOF) method with MCrAlY powder. Two of the samples were coated with a 300 μm topcoat. The other two were coated with a 200 μm and the rest two were coated with a 400 μm topcoat, respectively. The heating test was performed using an electric furnace with a capacity of 1400 °C. Six coated samples are heated to 1100 °C in the furnace and the dwell period was 75 h. The furnace was specially designed with an observation window to momentarily observe the states of the samples. After 75 h at 1100 °C, the six specimens were cooled down in the furnace. The samples and the testing equipment are shown in Figure 26.

TC spallation was found in three of the specimens. The specimens with a 200 μm TC were all undamaged. One of the 300 μm TC and two 400 μm TC spalled from the specimens after cooling to room temperature. During the heating-dwell-cooling period, the specimens did not fail. The spallation of TC occurred after being kept at room temperature for some time. The specimens before and after experiments are shown in Figure 26. The present study confirmed the prediction that the TBC systems with thicker TC are more likely to fail when cooling down from the elevated temperature.

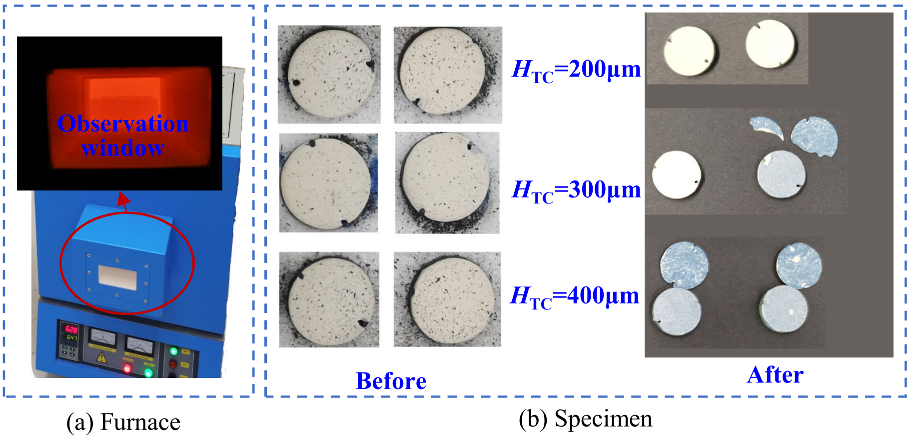


**Figure 26.** The furnace and specimen before and after heating–cooling experiments.

## 4. Discussion

A separation at the layer interface occurs when either the tensile stress perpendicular to the interface exceeds a critical value $\sigma_{c,i}$ or the interfacial shear stress exceeds a critical value $\tau_{c,i}$. If the interfacial normal stress exceeds $\sigma_{c,i}$, then a mode I fracture is more likely to form, while a mode II fracture is always caused by shear stress [24]. When the normal stress parallel to the interface exceeds $\sigma_{c,i}$, the crack perpendicular to the interface may grow and create new free edges inside the system. Schematic illustrations of mode I and mode II fractures are shown in Figure 27.

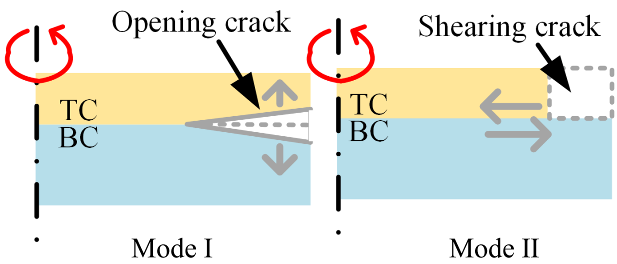


**Figure 27.** Illustration of two fracture modes.

Assuming that the coating–substrate system contains no cracks, spalling occurs at the edge. The precise prediction of the failure of coating–substrate systems requires the accurate analysis of the stress state near the edge. Although the stress near the edge is singular, increasing the grid density is beneficial to the accuracy of the stress distribution. The application of a submodel in the FEM is effective in dealing with the complicated coating–substrate system since the region of stress concentration can be modeled separately with a finer mesh. The size of the submodel can be determined by the parameter $d_{A_2}/H_{TC}$, i.e., the ratio of the distance from the edge to point $A_2$ where the shear stress reaches zero and remains unchanged. If the distance from a specific edge to a point in the structure is greater than $d_{A_2}$, then the position is regarded as unaffected by the concerned edge. Different coating–substrate systems correspond to different geometric and material variations, and the parameter $d_{A_2}/H_{TC}$ changes with the system. From Figure 17, as the elastic modulus and Poisson's ratio of the TC increase, $d_{A_2}/H_{TC}$ approaches 12. The existence of TGO does not have a significant effect on the parameter $d_{A_2}/H_{TC}$.

The results from the calculation of $\psi_1$ and $\psi_2$ under various conditions are listed in Table 7. The $\psi_1$ for the disk with or without TGO at elevated temperature (i.e., $\Delta T$ is positive) are negative. Whereas the $\psi_1$ at ambient temperature (i.e., $\Delta T$ is negative) are positive, indicating that opening mode I edge delamination may occur at ambient temperature. Previous studies have shown that a large thermal difference and large CTE difference lead to high stresses near the edge. The coating–substrate system works at elevated temperatures, and TGO is formed in service. When the machine is shut down or the specimen is removed from the furnace, the temperature drops to room temperature, which is below the 'stress-free temperature', $\psi_1$ becomes positive, and mode I delamination is promoted on the interface between the TC and TGO. The higher the temperature at which the disk is heated, the more severe damage the disk may undergo. Moreover, the larger the strain difference, the larger the $\psi_2$, indicating the more server mode II failure.

Figures 15 and 16 illustrate that the region where the free edge effects occur is related to the elastic modulus. Poisson's ratio slightly affects the size of this region. The stress magnitude close to the free edge depends on both material properties. The elastic modulus and Poisson's ratio depend on the specimen preparation process. The elastic modulus is smaller for the TC prepared by APS than by EB-PVD [48]. Poisson's ratio of the TC prepared by EB-PVD is larger [40,49]. When the disk spends a long time at elevated temperatures, the elastic modulus of the TC becomes larger due to sintering [50] and corrosion [51]. The region where the free edge is influential is larger for the system in which the elastic modulus and Poisson's ratio are higher. The stress and the integral parameters also increase with increasing elastic modulus and Poisson's ratio of the TC. This may promote mode I and II delamination.

As the thickness of the TC increases from 100 μm to 1500 μm, the value of $\psi_1$ increases 72-fold, and the value of $\psi_2$ increases 5-fold. With increasing thickness of the BC from 100 μm to 500 μm, the maximum interfacial stress at the edge decreases by less than 1%. As the thickness of the TGO increases from 1 μm to 8 μm, the value of $\psi_1$ decreases by 29.4%, and the value of $\psi_2$ decreases by 28.7%. As the elastic modulus of TC increases from 15 GPa to 100 GPa, the value of $\psi_1$ increases 4-fold, and the value of $\psi_2$ increases 4-fold. As the Poisson's ratio of TC increases from 0 to 0.25, the value of $\psi_1$ increases by 23.2%, and the value of $\psi_2$ increases by 23.8%. Through the comparison and analysis, the thickness of BC has less effect. Both the thickness and the elastic modulus of TC are more effective. The two parameters are further compared by increasing the same multiple. As the thickness of the TC increases from 400 μm to 1000 μm, the value of $\psi_1$ increases 3-fold. As the elastic modulus of TC increases from 40 GPa to 100 GPa, the value of $\psi_1$ increases by 106%. The thickness of the TC is the most effective parameter.

**Table 7.** Calculated results of $\psi_1$ and $\psi_2$ of the cases in Section 3 under different conditions.

| | Case 1 | | | Case 2 | | | Case 3 | |
|---|---|---|---|---|---|---|---|---|
| $\Delta T$ °C | $\psi_1$ /N·mm | $\psi_2$ /N | $\nu_{TC}$ | $\psi_1$ /N·mm | $\psi_2$ /N | $E_{TC}$ /GPa | $\psi_1$ /N·mm | $\psi_2$ /N |
| −100 | 21.614 | 108.597 | 0.25 | 22.623 | 113.794 | 100 | 25.843 | 129.881 |
| 100 | −21.614 | 108.597 | 0.20 | 21.614 | 108.597 | 80 | 21.973 | 110.272 |
| 300 | −64.843 | 325.792 | 0.15 | 20.694 | 103.866 | 70 | 19.851 | 99.540 |
| 500 | −108.071 | 542.986 | 0.10 | 19.851 | 99.540 | 40 | 12.569 | 62.878 |
| 800 | −172.914 | 868.777 | 0.05 | 19.076 | 95.568 | 25 | 8.305 | 41.734 |
| - | - | - | 0 | 18.367 | 91.909 | 15 | 5.201 | 26.371 |
| | Case 4 | | | Case 5 | | | Case 6 | |
| $H_{TC}$ /μm | $\psi_1$ /N·mm | $\psi_2$ /N | $H_{TGO}$ /μm | $\psi_1$ /N·mm | $\psi_2$ /N | $H_{TC}$ /μm | $\psi_1$ /N·mm | $\psi_2$ /N |
| 1500 | 129.919 | 197.703 | 1 | 37.354 | 187.951 | 1000 | 132.226 | 282.081 |
| 1000 | 85.727 | 180.261 | 3 | 34.076 | 171.655 | 500 | 49.345 | 199.956 |
| 500 | 31.393 | 126.712 | 5 | 30.500 | 154.320 | 400 | 34.076 | 171.655 |
| 400 | 21.614 | 108.597 | 8 | 26.366 | 134.032 | 200 | 9.880 | 98.696 |
| 200 | 6.248 | 62.587 | - | - | - | 100 | 2.673 | 52.901 |
| 100 | 1.790 | 35.986 | - | - | - | - | - | - |

The models in cases 1–4 have no TGO. Case 1: The temperature difference is varied. Case 2: The Poisson's ratio of the TC is varied and $E_{TC}$ = 70 GPa, $\Delta T = -100$ °C. Case 3: The elastic modulus of the TC is varied and $\nu_{TC}$ = 0.1, $\Delta T = -100$ °C. Case 4: The thickness of the TC is varied, $\Delta T = -100$ °C. Case 5: The thickness of the TGO is varied, $H_{TC} = 400$ μm and $T$ = 20 °C. Case 6: The thickness of the TC is varied, $H_{TGO} = 3$ μm and $T$ = 20 °C.

With the growth of the TGO, the interfacial normal and shear stress near the free edge increases (as shown in Figure 13). In contrast, the integral value $\psi$ decreases slightly with the increasing thickness of TGO. With the increasing TGO thickness, the adhesion ability between TGO and TC/BC declines. Assuming that the larger the integral value $\psi$ is, the TC is more likely to spall. In other words, when the best balance is reached between the interfacial stresses and the adhesion ability, the formation of TGO is beneficial for thermal shock resistance. The effect of TGO thickness on the thermal shock resistance of TBCs was evaluated by Torkashvand [52]. The results demonstrated that the presence of TGO with a thickness of 2–3 μm has a positive effect on the resistance against thermal shock.

Creep deformation due to high temperature [40], the pressure difference between inside and outside surfaces [53], and the thermal gradient [54] in service also have significant effects on the interfacial stress. However, they are not considered in the analysis. These are directions for future research.

## 5. Conclusions

By using both analytical and finite element methods, this study models the stress state in disks with ordinary bilayer thermal barrier coatings. A mathematical model is developed to determine the parameters affecting the interfacial stress of the system with thick coatings. An FEM model is utilized to quantitatively investigate the effects of the abovementioned characteristics. Two integral parameters are proposed to quantify the strain mismatch in coating–substrate systems. The main conclusions are as follows:

(1) The CTE, elastic modulus, Poisson's ratio, and thickness of each layer are the material and geometric characteristics that affect the interfacial stress. Through the comparison and analysis, the thickness of BC has less effect and the thickness of the TC has the biggest influence on the interfacial stress.
(2) The elastic modulus and Poisson's ratio are essential in determining the magnitude of the interfacial stress and the distribution of the stress curve. The magnitude of the interfacial stress increases with increasing elastic modulus and Poisson's ratio of the TC. The region affected by free edges also becomes larger with increasing elastic modulus and Poisson's ratio of the TC. However, the distance between the free edge and the point at which the maximum interfacial shear stress occurs increases with increasing elastic modulus and decreases with increasing Poisson's ratio.
(3) The TGO significantly influences the distribution of the interfacial stress at the TC boundary. At ambient temperature, when TGO forms, the stress state near the free edge is tensile instead of compressive. This dangerous condition will occur at ambient temperature. The heating–cooling experiments proved this point. EDS was carried out to examine the element content in the spalling TC part and the rest part. The picture and data from EDS indicate that the separation mainly occurs at the interface between TC and TGO. With the growth of TGO, the interfacial stress near the edge increases.
(4) With the nondimensional parameter $d/H_{\mathrm{TC}}$, the curve of the interfacial stress between the TC and BC/TGO can be consolidated into a parameter. Then, the proposed integral value can represent the stress state near a free edge and is related to mode I and II fracture mechanics (i.e., the delamination of the interface). The parameters indicate that the TBC systems with thicker topcoats are more likely to fail due to strain mismatch. The heating–cooling test bears this out.

**Author Contributions:** Q.T.: Methodology, Validation, Writing—original draft preparation. Y.W.: Conceptualization, Supervision, Writing—review and editing. S.Y.: Project administration, Writing—review and editing. Y.L.: Methodology, Validation. All authors have read and agreed to the published version of the manuscript.

**Funding:** This research was funded by the National Science and Technology Major Project grant number J2019-Ⅳ-0006-0074 and the National Natural Science Foundation of China (No.12202030).

**Institutional Review Board Statement:** Not applicable.

**Data Availability Statement:** Data in the paper are available from the authors.

**Acknowledgments:** The authors sincerely appreciate the scholars from the Institute of Engineering Thermophysics of Chinese Academy of Sciences for their valuable discussion and Chen-Hong Du and Tong-Hui Wang for their help in formula deduction.

**Conflicts of Interest:** The authors declare no conflict of interest.

## Abbreviations

The following abbreviations are used in this manuscript:

| | |
|---|---|
| APS | Air Plasma Spraying |
| A.S. | Analytical Solution |
| BC | Bondcoat |
| EB-PVD | Electron Beam Physical Vapor Deposition |
| EDS | Energy Disperse Spectroscopy |
| FEM | Finite Element Method |
| SEM | Scanning Electron Microscopy |
| TBC | Thermal Barrier Coatings |
| TC | Topcoat |
| TGO | Thermal Grown Oxide |

## Nomenclature

| | |
|---|---|
| $a$ | an intermediate variable related to the thickness of the layers |
| $d$ | distance from a point on the interface to the edge of the disk-shaped coating–substrate system, μm |
| $x$ | the radial direction |
| $y$ | the axial direction |
| $z$ | the circumferential direction |
| $E$ | the elastic modulus, GPa |
| $F$ | the total internal force of the layer per length, N/m |
| $H$ | the thickness of the layers, μm |
| $M$ | the moment of force, N·m |
| $T$ | the temperature, °C |
| $\alpha$ | the coefficient of thermal expansion (CTE), $°C^{-1}$ |
| $\delta$ | the distance from the point at which the maximum shear stress occurs to the edge of the disk-shaped coating–substrate system, μm |
| $\varepsilon$ | the total strain |
| $\varepsilon^{t}$ | the thermal strain |
| $\lambda$ | the coefficient of axial compliance |
| $\nu$ | Poisson's ratio |
| $\xi$ | the ratio of the distance from the point to the edge to the thickness of the TC layer |
| $\rho$ | the radius of curvature of the system, μm |
| $\sigma_{\mathrm{n}}$ | the interfacial normal stress, MPa |
| $\sigma_x$ | the radial stress, MPa |
| $\sigma_y$ | the axial stress, MPa |
| $\sigma_z$ | the hoop stress, MPa |
| $\tau_{xy}$ | the interfacial shear stress, MPa |
| $\psi_1$ | an integral value related to the interfacial normal stress near the free edge, N·mm |
| $\psi_2$ | an integral value related to the interfacial shear stress near the free edge, N |

## Appendix A. Analytical Solutions of Thermal Mismatch Stress

The main equations of each analytical solution dealing with the thermal mismatch stress are listed in the table below.

**Table A1.** Review of the analytical solutions to stress due to the thermal mismatch.

| Geometric Model | Equations | Nomenclature |
|---|---|---|
| A multilayered heteroepitaxial structure [20] | Normal stress parallel to the interface: $\sigma_i = \frac{E_i h_i \Delta\alpha_i \Delta T}{1-v_i}$<br>Interfacial shear stress:<br>$\tau_i(x) = -k\Delta T\left(\sum_{j=i}^{m} \frac{E_j h_j \Delta\alpha_j}{1-v_j}\right)\frac{\cosh kx}{\cosh kl}$<br>Interfacial peeling stress:<br>$p_i(x) = -\frac{1}{2}k^2\Delta T\left(\sum_{j=i}^{m} \frac{E_j h_j \Delta\alpha_j}{1-v_j}\right)\frac{\cosh kx}{\cosh kl}\sum_{j=i+1}^{m} h_j$<br>$k = \sqrt{\frac{3\sum_{i=0}^{m}\frac{(1-v_i)}{E_i h_i}}{4\sum_{i=0}^{m}\frac{h_i(1-v_i)}{E_i}}}$ | $l$ half of the film's length<br>$x$ the distance from the center of the film to the point<br>$m$ the number of film layers<br>$i$ the '$i$'th layer<br>$\Delta T$ the temperature difference<br>$\Delta\alpha_i$ the difference between the CTE of the film and the substrate<br>'0' substrate |
| A circular substrate/thin-film structure [21] | Radial stress: $\sigma_{ri} = \frac{E_i \Delta\alpha_i \Delta T}{1-v_i}\left[1 - \frac{kaI_0(kr)-(1-v_i)R\frac{I_1(kr)}{r}}{kaI_0(kR)-(1-v_i)I_1(kR)}\right]$<br>Hoop stress: $\sigma_{\theta i} = \frac{E_i \Delta\alpha_i \Delta T}{1-v_i}\left[1 - \frac{v_i kaI_0(kr)+(1-v_i)R\frac{I_1(kr)}{r}}{kRI_0(kR)-(1-v_i)I_1(kR)}\right]$<br>Interfacial shear stress:<br>$\tau_i(r) = \frac{3E_0(1+v_i)\sum_{i=1}^{m}\frac{E_i h_i \Delta\alpha_i \Delta T}{1-v_i} RI_1(kr)}{2(1+v_0)h_0[kRI_0(kR)-(1-v_i)I_1(kR)]\left(\sum_{i=1}^{m}\frac{E_i h_i}{1-v_i}\right)}$<br>$k = \sqrt{\frac{3E_0}{2(1+v_0)h_0\sum_{i=1}^{m}\frac{E_i h_i}{1-v_i^2}}}$ | $I_n(\cdot)$ the modified Bessel function<br>$R$ the radius of the disk<br>$r$ the distance from the center of the disk to the point |
| An elastic multilayered strip [26] | Normal stress parallel to the interface in the substrate:<br>$\sigma_0 = \frac{2}{h_0^2}\left(3y + 2h_0 - \frac{2}{E_0}\sum_{j=1}^{m} E_j h_j\right)\sum_{k=1}^{m} E_k h_k \Delta\alpha_k \Delta T$<br>Normal stress parallel to the interface in the "i'th film:<br>$\sigma_i = E_i\left[-\Delta\alpha_i + 4\sum_{j=1}^{m}\frac{E_j h_j \Delta\alpha_j}{E_0 h_0}\right]\Delta T$ | |
| An elastic thin disk model with a hole in the middle [31] | Radial stress:<br>$\sigma_r = -\frac{E}{1-v^2}\left(\frac{d^2w}{dx^2} + \frac{v}{x}\cdot\frac{dw}{dx}\right)\cdot(y+\delta_r) + \frac{E}{1-v}(c-\varepsilon_T)$<br>Hoop stress:<br>$\sigma_\theta = -\frac{E}{1-v^2}\left(\frac{1}{x}\cdot\frac{dw}{dx} + v\frac{d^2w}{dx^2}\right)\cdot(y+\delta_r) + \frac{E}{1-v}(c-\varepsilon_T)$<br>$c = \frac{\sum_{i=0}^{n}\frac{E_i h_i}{1-v_i}\varepsilon_T^i dz}{\sum_{i=0}^{n}\frac{E_i h_i}{1-v_i}}$<br>$\delta_r = -\frac{\sum_{i=0}^{n}\frac{E_i\left(y_i^2-y_{i-1}^2\right)}{1-v_i}\left(1+\frac{1-v_i}{1+v_i}\frac{R^2}{x^2}\right)}{\sum_{i=0}^{n}\frac{2E_i h_i}{1-v_i}\left(1+\frac{1-v_i}{1+v_i}\frac{b^2}{x^2}\right)}$<br>$w = A_1\left[x^2 - 2R^2\ln(x/R) - R^2\right]$<br>$A_1 = \frac{\sum_{i=0}^{n}\frac{E_i}{1-v_i}\left(c-\varepsilon_T^i\right)(y_{i-1}+h_i/2+\delta_{r=a})}{\sum_{i=0}^{n}\frac{2E_i}{1-v_i}\left(1+\frac{1-v_i}{1+v_i}\frac{R^2}{R_{\mathrm{h}}^2}\right)\cdot\frac{\left(y_i+\delta_{r=a}\right)^3-\left(y_{i-1}+\delta_{r=a}\right)^3}{3}}$ | $c$ the uniform strain<br>$\delta_{\mathrm{r}}$ the location of the bending axis<br>$w$ the bending deflection<br>$\varepsilon_{\mathrm{T}}$ the thermal strain |

## References

1. Darolia, R. Thermal barrier coatings technology: Critical review, progress update, remaining challenges and prospects. *Int. Mater. Rev.* **2013**, *58*, 315–348. [CrossRef]
2. Kumar, V.; Balasubramanian, K. Progress update on failure mechanisms of advanced thermal barrier coatings: A review. *Prog. Org. Coat.* **2016**, *90*, 54–82. [CrossRef]
3. Mehboob, G.; Liu, M.J.; Xu, T.; Hussain, S.; Mehboob, G.; Tahir, A. A review on failure mechanism of thermal barrier coatings and strategies to extend their lifetime. *Ceram. Int.* **2020**, *46*, 8497–8521. [CrossRef]
4. Mensch, A.; Thole, K.A.; Craven, B.A. Conjugate heat transfer measurements and predictions of a blade endwall with a thermal barrier coating. *J. Turbomach.* **2014**, *136*, 121003. [CrossRef]
5. Liu, Q.M.; Huang, S.Z.; He, A.J. Composite ceramics thermal barrier coatings of yttria stabilized zirconia for aero-engines. *J. Mater. Sci. Technol.* **2019**, *35*, 2814–2823. [CrossRef]
6. Yang, S. Multiscale modeling of chemo-thermo-mechanical damage of EB-PVD thermal barrier coatings. *J. Mech. Phys. Solids* **2022**, *158*, 104667. [CrossRef]

7. Yang, S.; Yuan, H.; Zeng, W.; Guo, H. Chemo-thermo-mechanical modeling of EB-PVD TBC failure subjected to isothermal and cyclic thermal exposures. *Int. J. Fatigue* **2020**, *141*, 105817. [CrossRef]
8. Yang, S.; Yuan, H. Characterization of isothermal and cyclic thermal damage of EB-PVD TBCs with the help of the 3D-DIC technique. *Fatigue Fract. Eng. Mater. Struct.* **2022**, *45*, 186–202. [CrossRef]
9. Sun, J.Y.; Yang, S.; Yuan, H. Assessment of thermo-mechanical fatigue in a nickel-based single-crystal superalloy CMSX-4 accounting for temperature gradient effects. *Mater. Sci. Eng. A* **2021**, *809*, 140918. [CrossRef]
10. Jiang, J.S.; Ma, X.F.; Wang, B. Stress analysis of the thermal barrier coating system near a cooling hole considering the free-edge effect. *Ceram. Int.* **2020**, *46*, 331–342. [CrossRef]
11. Gildersleeve, V.E.J.; Nakamura, T.; Sampath, S. Durability of plasma sprayed Thermal Barrier Coatings with controlled properties part II: Effects of geometrical curvature. *Surf. Coat. Technol.* **2021**, *424*, 127671. [CrossRef]
12. Hardwicke, C.U.; Lau, Y.C. Advances in thermal spray coatings for gas turbines and energy generation: A review. *J. Therm. Spray Technol.* **2013**, *22*, 564–576. [CrossRef]
13. Yang, S.; Peng, H.; Zhang, T. A damage model to evaluate the mechanical properties in the medium -long life stage for coating system subjected to elevated thermal loads with 3D-DIC technique. *J. Alloys Compd.* **2020**, *832*, 154955. [CrossRef]
14. Kim, D.H.; Kim, K.K.; Moon, B.W.; Park, K.B.; Park, S.; Seok, C.S. Prediction of growth behavior of thermally grown oxide considering the microstructure characteristics of the top coating. *Ceram. Int.* **2021**, *47*, 14160–14167. [CrossRef]
15. Stoney, G.G. The Tension of Metallic Films Deposited by Electrolysis. *Proc. R. Soc. Lond.* **1909**, *82*, 172–175.
16. Zhang, X.C.; Watanabe, M.; Kuroda, S. Effects of processing conditions on the mechanical properties and deformation behaviors of plasma-sprayed thermal barrier coatings: Evaluation of residual stresses and mechanical properties of thermal barrier coatings on the basis of in situ curvature measurement under a wide range of spray parameters. *Acta Mater.* **2013**, *61*, 1037–1047. [CrossRef]
17. Song, Y.; Zhuan, X.; Wang, T.J.; Chen, X. Evolution of thermal stress in a coating/substrate system during the cooling process of fabrication. *Mech. Mater.* **2014**, *74*, 26–40. [CrossRef]
18. Mao, W.G.; Chen, Y.Y.; Wang, Y.J.; Zhou, M.; Yang, H.Y.; Wang, Z.; Dai, C.Y.; Chen, X.; Fang, D.N. A multilayer structure shear lag model applied in the tensile fracture characteristics of supersonic plasma sprayed thermal barrier coating systems based on digital image correlation. *Surf. Coat. Technol.* **2018**, *350*, 211–226. [CrossRef]
19. Song, Y.; Wu, W.; Qin, M.; Li, D.; Liu, Y.; Ai, S.; Wang, T.J. Effect of geometric parameter on thermal stress generation in fabrication process of double-ceramic-layers thermal barrier coating system. *J. Eur. Ceram. Soc.* **2018**, *38*, 3962–3973. [CrossRef]
20. Suhir, E. An approximate analysis of stresses in multilayered elastic thin films. *J. Appl. Phys.* **1988**, *55*, 143–148. [CrossRef]
21. Suhir, E. Predicted thermally induced stresses in, and the bow of, a circular substrate/thin-film structure. *J. Appl. Phys.* **2000**, *88*, 2363–2370. [CrossRef]
22. Zhang, X.C.; Xu, B.S.; Wang, H.D.; Wu, Y.X. Analytical modeling of edge effects on the residual stresses within the film/substrate systems. I. Interfacial stresses. *J. Appl. Phys.* **2006**, *100*, 113524. [CrossRef]
23. Chou, T.L.; Yang, S.Y.; Chiang, K.N. Overview and applicability of residual stress estimation of film-substrate structure. *Thin Solid Films* **2011**, *519*, 7883–7894. [CrossRef]
24. Teixeira, V. Mechanical integrity in PVD coatings due to the presence of residual stresses. *Thin Solid Films* **2001**, *392*, 276–281. [CrossRef]
25. Hu, S.M. Film-edge-induced stress in substrates. *J. Appl. Phys.* **1979**, *50*, 4661–4666. [CrossRef]
26. Hsueh, C.H. Thermal stresses in elastic multilayer systems. *Thin Solid Films* **2002**, *418*, 182–188. [CrossRef]
27. Hsueh, C.H.; Luttrell, C.R.; Lee, S.; Wu, T.C.; Lin, H.Y. Interfacial peeling moments and shear forces at free edges of multilayers subjected to thermal stresses. *J. Am. Ceram. Soc.* **2006**, *89*, 1632–1638. [CrossRef]
28. Hu, Y.Y.; Huang, W.M. Elastic and elastic-plastic analysis of multilayer thin films: Closed-form solutions. *J. Appl. Phys.* **2004**, *96*, 4154–4160. [CrossRef]
29. Huang, W.M.; Hu, Y.Y.; An, L. A simple approach to determine five thermomechanical properties of thin ductile films on an elastic substrate. *Appl. Phys. Lett.* **2004**, *85*, 6173–6175. [CrossRef]
30. Gao, C.X.; Zhao, Z.W.; Li, X.H. Modeling of thermal stresses in elastic multilayer coating systems. *J. Appl. Phys.* **2015**, *117*, 055305. [CrossRef]
31. Meng, Z.W.; Liu, Y.B.; Li, Y.J.; Zhang, Y.S. An analytical model for predicting residual stress in TBC-film cooling system considering non-uniform temperature field. *J. Appl. Phys.* **2021**, *129*, 135301. [CrossRef]
32. Tsui, Y.C.; Clyne, T.W. An analytical model for predicting residual stresses in progressively deposited coatings. Part 1: Planar geometry. *Thin Solid Films* **1997**, *306*, 23–33. [CrossRef]
33. Tsui, Y.C.; Clyne, T.W. An analytical model for predicting residual stresses in progressively deposited coatings Part 2: Cylindrical geometry. *Thin Solid Films* **1997**, *306*, 34–51. [CrossRef]
34. Tsui, Y.; Clyne, T. An analytical model for predicting residual stresses in progressively deposited coatings Part 3: Further development and applications. *Thin Solid Films* **1997**, *306*, 34–51. [CrossRef]
35. Moore, T.D. Thermomechanical peeling in multilayer beams and plates—A solution from first principles. *Int. J. Solids Struct.* **2005**, *42*, 271–285. [CrossRef]
36. Widjaja, S.; Limarga, A.M.; Yip, T.H. Modeling of residual stresses in a plasma-sprayed zirconia/alumina functionally graded-thermal barrier coating. *Thin Solid Films* **2003**, *434*, 216–227. [CrossRef]

37. Jiang, J.S.; Wu, D.; Wang, W.Z.; Zhao, X.F.; Ma, X.F.; Wang, B.; Shi, H.J. Fracture behavior of TBCs with cooling hole structure under cyclic thermal loadings. *Ceram. Int.* **2020**, *46*, 3644–3654. [CrossRef]
38. Dolgov, N.A. Analytical methods to determine the stress state in the substrate-coating system under mechanical loads. *Strength Mater.* **2016**, *48*, 658–667. [CrossRef]
39. Agrawal, D.C.; Raj, R. Measurement of the ultimate shear strength of a metal-ceramic interface. *Acta Metall.* **1989**, *37*, 1265–1270. [CrossRef]
40. Ali, M.Y.; Nusier, S.Q.; Newaz, G.M. Creep effects on early damage initiation in a TBC system. *J. Mater. Sci.* **2004**, *39*, 3383–3390. .:JMSC.0000026940.56103.d3. [CrossRef]
41. Academic Committee of Superalloys. *China Superalloys Handbook*; Standards Press of China: Beijing, China, 2012.
42. Li, D.J.; Y, Y.L.; F, S.; P, J.; W, C.Y.; J, W.T. Effect of preheating temperature on formation of surface cracks in thermal barrier coating system. *Acta Aeronaut. Astronaut. Sin.* **2022**, *43*, 516184. (In Chinese)
43. Karaoglanli, A.C.; Grund, T.; Turk, A.; Lampke, T. A comparative study of oxidation kinetics and thermal cyclic performance of thermal barrier coatings (TBCs). *Surf. Coat. Technol.* **2019**, *371*, 47–67. [CrossRef]
44. Rosler, J.; Baker, M.; Aufzug, K. A parametric study of the stress state of thermal barrier coatings—Part I: Creep relaxation. *Acta Mater.* **2004**, *52*, 4809–4817. [CrossRef]
45. Nayebpashaee, N.; Seyedein, S.H.; Aboutalebi, M.R.; Sarpoolaky, H.; Hadavi, S.M.M. Finite element simulation of residual stress and failure mechanism in plasma sprayed thermal barrier coatings using actual microstructure as the representative volume. *Surf. Coat. Technol.* **2016**, *291*, 103–114. [CrossRef]
46. Clarke, D.R. The lateral growth strain accompanying the formation of a thermally grown oxide. *Acta Mater.* **2003**, *51*, 1393–1407. [CrossRef]
47. Wang, F.H.; Wang, Y.J.; Wu, Y.X. Prediction of thermal growth stress in thermal barrier coating system. *Rare Met. Mater. Eng.* **2010**, *39*, 2122–2126.
48. Patsias, S.; Tassini, N.; Lambrinou, K. Ceramic coatings: Effect of deposition method on damping and modulus of elasticity for yttria-stabilized zirconia. *Mater. Sci. Eng. A* **2006**, *442*, 504–508. [CrossRef]
49. Kyaw, S.; Jones, A.; Hyde, T. Predicting failure within TBC system: Finite element simulation of stress within TBC system as affected by sintering of APS TBC, geometry of substrate and creep of TGO. *Eng. Failure Anal.* **2013**, *27*, 150–164. [CrossRef]
50. Ahrens, M.; Lampenscherf, S.; Vassen, R.; Stover, D. Sintering and creep processes in plasma-sprayed thermal barrier coatings. *J. Therm. Spray Technol.* **2004**, *13*, 432–442. [CrossRef]
51. Kakuda, T.R.; Levi, C.G.; Bennett, T.D. The thermal behavior of CMAS-infiltrated thermal barrier coatings. *Surf. Coat. Technol.* **2015**, *272*, 350–356. [CrossRef]
52. Torkashvand, K.; Poursaeidi, E.; Mohammadi, M. Effect of TGO thickness on the thermal barrier coatings life under thermal shock and thermal cycle loading. *Ceram. Int.* **2018**, *44*, 9283–9293. [CrossRef]
53. Talebitooti, R.; Gohari, H.D.; Zarastvand, M.R. Multi objective optimization of sound transmission across laminated composite cylindrical shell lined with porous core investigating non-dominated sorting genetic algorithm. *Aerosp. Sci. Technol.* **2017**, *69*, 269–280. [CrossRef]
54. Rahmatnezhad, K.; Zarastvand, M.R.; Talebitooti, R. Mechanism study and power transmission feature of acoustically stimulated and thermally loaded composite shell structures with double curvature. *Compos. Struct.* **2021**, *276*, 114557. [CrossRef]